Draft for submission to Icarus

Wrinkle ridges on Mercury and the Moon within and outside of mascons

Lisa S. Schleicher[1], Thomas R. Watters[1], Aaron J. Martin[2], and Maria E. Banks[1,3]

[1]Center for Earth and Planetary Studies, National Air and Space Museum, Smithsonian Institution, Washington, DC 20560, USA.

[2]División de Geociencias Aplicadas, IPICYT, CP. 78216 San Luis Potosí, SLP, MÉXICO.

[3]NASA Goddard Space Flight Center, Greenbelt, MD 20771, USA.

*Corresponding Author: Lisa S. Schleicher, phone: 832-768-1262

email: lisasschleicher@gmail.com

Keywords: wrinkle ridges, global contraction, subsidence, relief, tectonic surface deformation

Components: 33 pages, 10 figures, 2 tables

Auxiliary Material: 1 document, 3 tables

ABSTRACT

Found on all terrestrial planets, wrinkle ridges are anticlines formed by thrust faulting and folding resulting from crustal shortening. The MErcury Surface, Space Environment, Geochemistry, and Ranging (MESSENGER) spacecraft's orbital phase returned high resolution images and topographic data of the previously unimaged northern high latitudes of Mercury where there are large expanses of smooth plains deformed by wrinkle ridges. Concurrently, the Lunar Reconnaissance Orbiter (LRO) is obtaining high resolution images and topographic data covering lunar mare wrinkle ridges. These data allow quantitative comparison of the scale of wrinkle ridges in smooth plains volcanic units on Mercury with mare wrinkle ridges. We evaluate the topographic relief of 300 wrinkle ridges within and outside of mascons basins on the Moon and Mercury. The relief of wrinkle ridges measured ranges from ~112 to 776 m with a mean relief of ~350 m (median = ~340 m, n = 150) on Mercury and ~47 to 678 m with a mean relief of ~198 m (median = ~168 m, n = 150) on the Moon. Wrinkle ridges on Mercury thus are approximately twice as large in mean relief compared to their counterparts on the Moon. The larger scale of Mercury's wrinkle ridges suggests that their formation can be attributed, in part, to global contraction. As global contraction on the Moon is estimated to be an order of magnitude smaller than on Mercury, the smaller scale of lunar wrinkle ridges suggests they most likely form primarily by load induced subsidence of the mare basalt. The relief of wrinkle ridges located in lunar mascon basins and in the Caloris mascon on Mercury are not statistically significantly different than ridges in non-mascon regions, suggesting comparable levels of contractional strain. The fact that mascon basins do not host wrinkle ridges with greater structural relief relative to non-mascon units may indicate the critical role lithospheric thickness

plays in controlling subsidence and contraction of thick volcanic sequences on the Moon and Mercury.

1. Introduction

On March 18, 2011 the MErcury Surface, Space Environment, Geochemistry, and Ranging (MESSENGER) spacecraft transitioned from orbiting the Sun to being the first spacecraft to orbit Mercury. Meanwhile, the Lunar Reconnaissance Orbiter (LRO) has been orbiting the Moon since June 2009. Crustal shortening on Mercury and the Moon is expressed by lobate scarps, wrinkle ridges, and on Mercury, high-relief ridges [*Watters et al.*, 2009a; *Watters and Johnston*, 2010; *Watters and Nimmo*, 2010]. Recently obtained orbital images and altimetry data from both LRO and MESSENGER offer an unprecedented opportunity to characterize the morphometry of these tectonic features. This study focuses on a quantitative characterization of wrinkle ridges, contractional tectonic features found in mare basalt on the Moon and smooth plains volcanic material on Mercury, whichformed from a combination of thrust faulting and folding [*Strom*, 1970; *Maxwell et al.*, 1975; *Strom et al.*, 1975; *Solomon and Head*, 1979; *Plescia and Golombek*, 1986; *Watters*, 1988; *Watters et al.*, 2009c; 2010].

Images obtained by MESSENGER show that a significant amount of Mercury's surface, almost 27%, is covered by smooth plains [*Denevi et al.*, 2013]. The greatest expanse of smooth plains material on Mercury is in the northern high-latitudes, covering ~6% of the surface (Figures 1 and 2) [*Head et al.*, 2011]. On the Moon, mare basalt covers ~15% of the nearside and ~1% of the farside surface [Nelson et al. 2014]. The smooth plains material on Mercury is likely volcanic in origin and has a basalt-like composition [*Nittler et al.*, 2011; *Denevi et al.*, 2013], and likely consists of a multilayered sequence of lava flows.

The following data from MESSENGER and LRO, enable us to more accurately identify, map, and quantitatively compare wrinkle ridges on Mercury and the Moon: (1) high resolution images and altimetry data, respectively, from the Mercury Dual Imaging System (MDIS) [*Hawkins et al.,* 2007] and Mercury Laser Altimeter (MLA) [*Zuber et al.,* 2013] aboard MESSENGER and the Lunar Reconnaissance Orbiter Camera (LROC) [*Robinson et al*., 2010] and Lunar Orbiter Laser Altimeter (LOLA) [*Smith et al*., 2010] aboard LRO, (2) global image mosaics and stereo-image derived regional and global topography datasets for Mercury and the Moon, and (3) nearly global high-incidence angle (65 to 88°) imaging of Mercury. These datasets and their resolution are described in detail below and in the Auxiliary Material. In this paper, we use these new datasets to perform a statistical comparison of the location and reliefs of 150 wrinkle ridges on each of these bodies. Examination of wrinkle ridges on Mercury and the Moon allows us to evaluate the influence of tectonic setting and global radial contraction in the formation of these landforms.

2. Background

Wrinkle ridges are one of the most ubiquitous tectonic features found on the Moon and the terrestrial planets. They are commonly characterized as anticlines formed by folding and thrust faulting resulting from crustal shortening [*Plescia and Golombek*, 1986; *Watters*, 1988; *Golombek et al.*, 1991; *Watters and Schultz*, 2010] and typically consist of a broad, low relief arch and a superimposed ridge [*Watters*, 1988; *Schultz*, 2000]. Wrinkle ridges are generally found in two physiographic settings: (1) the interiors of impact basins, and (2) on broad expansive plains [*Watters*, 1988; *Watters and Johnston*, 2010; *Watters and Nimmo*, 2010].

On the Moon, the mare basalt filled basins are associated with mascons or mass concentrations that are distinguished by positive free-air gravity anomalies (Figure 1) [*Melosh et al*., 2013; *Zuber et al*., 2013]. Recently obtained high-resolution gravity data returned by the Gravity Recovery and Interior Laboratory (GRAIL) spacecraft shows in remarkable detail the large positive anomalies of mascons associated with major impact basins (e.g. Mare Serenitatis, Imbrium, and Crisum), and are interpreted to be regions with an excess of subsurface mass [*Zuber et al*., 2012; *Melosh et al*., 2013]. On the Moon, wrinkle ridges were first recognized and mapped from Earth-based telescopic observations of the nearside [*Gilbert*, 1893; *Fielder*, 1961; *Baldwin*, 1965; 1970]. Wrinkle ridges are well studied on the Moon from Apollo era photography and LROC imaging and are confined to mare basalt [*Wilhelms and McCauley*, 1971; *McCauley*, 1975; *Watters*, 1988]. Basins with mascon signatures generally exhibit basin-concentric and basin-radial wrinkle ridges that are interpreted to have formed in response to localized contraction driven by subsidence and flexure of the lithosphere from the superisostatic loading of thick sequences of relatively dense mare basalt [*Solomon and Head*, 1979; *Freed et al.*, 2001; *Watters and Johnson*, 2010; *Zuber et al.*, 2013]. Other expanses of mare basalt, like those in Procellarium and Frigoris, do not exhibit mascon-like positive free-air gravity anomalies [*Zuber et al.,* 2013].

On Mercury, gravity data obtained by MESSENGER [*Smith et al.*, 2012] shows the Caloris basin has a large positive free-air anomaly, interpreted to be a mascon (Figure 1). However, like the Moon, the large expanses of smooth plains of the Caloris exterior plains and much of the northern smooth plains do not have mascon-like gravity anomalies. On Mercury, wrinkle ridges were observed in the interior smooth plains material, and the exterior annulus of smooth plains of the Caloris basin in images returned by Mariner 10 [*Strom et al.*, 1975; *Melosh* *and McKinnon*, 1988; *Watters et al.*, 2005; *Fassett et al.*, 2009; *Watters et al.*, 2005; 2009a; 2009b; 2009c; *Watters and Nimmo*, 2010] (Figure 3). The maximum relief of fourteen wrinkle ridges imaged by Mariner 10 were estimated using shadow measurements with limited accuracy [*Watters*, 1988]. In addition, Earth based radar altimetry used to measure the relief of seven wrinkle ridges in the smooth plains of Tir Planitia revealed arch-like structures with relief ranging 200 to 730 m and lengths up to 130 m long [*Harmon et al.*, 1986; *Watters*, 1988; *Watters and Nimmo*, 2010]. Although Mariner 10 and the MESSENGER flybys returned image coverage for almost 98% of Mercury, few observations existed in Mercury's north polar region until MESSENGER's orbital phase. MESSENGER's orbital observations revealed the existence of large expansive smooth plains material covering the north polar region, known as the northern smooth plains [*Head et al., 2011*; *Denevi et al*., 2013, *Klimczak et al*., 2012]. Mercury's northern smooth plains can be described as ridged plains due to the ubiquity of wrinkle ridges. Wrinkle ridges in the northern smooth plains are often localized by buried impact craters, known as ghost craters [*Head et al.*, 2011; *Klimczak et al.*, 2012; *Watters et al.*, 2012a].

While previous research and observations have enabled us to begin to understand tectonic deformation on Mercury and the Moon, high resolution images and altimetry data from MESSENGER and LRO enable us to quantitatively compare and contrast wrinkle ridges on these bodies. One of the most revealing expressions of the level of strain in a contractional tectonic landform is its structural relief. Absent erosional or other processes, the best estimate of structural relief is the topographic relief of the landform. It has been shown that topographic relief of contractional tectonic landforms involving thrust faults can be used to estimate the maximum, cumulative displacement on the faults [*Wojtal*, 1996; *Watters et al*., 2000]. Thus, all things being equal, the average relief of a population of contractional tectonic features is a reasonable measure of the contractional strain.

3. Methods

3.1 Relief comparisons

We measured the relief of 150 wrinkle ridges each on Mercury and the Moon using images and topographic data obtained by the MESSENGER and LRO spacecrafts. On Mercury, the study area includes wrinkle ridges in the northern smooth plains and the interior and exterior smooth plains of the Caloris basin (Figure 2, Table S1). We excluded from this study wrinkle ridges in the northern smooth plains obviously influenced by the presence of ghost craters [*Watters et al.,* 2012a; *Klimczak et al.*, 2012]. For the Moon, wrinkle ridges were investigated from all of the major mare basins, including: Mare Serenitatis, Mare Crisium, Mare Imbrium, Mare Frigoris, and Oceanus Procellarum, Mare Fecunditatis, Mare Tranquillitatis, Mare Nubium, Mare Humorum, and Mare Nectaris (Figure 4, Table S2).

The total population of wrinkle ridges on Mercury and the Moon were sub-sampled to examine the statistical difference between wrinkle ridges located in mascons versus wrinkle ridges in regions with no mascon-like gravity anomalies (Figures 1, 2, 3, and 4). On the Moon, we compare the dimensions of wrinkle ridges in the mascon basins (Mare Crisum, Mare Serenitatis, Mare Imbrium, Mare Humorum, and Mare Necataris) to wrinkle ridges in non-mascon environments (Mare Frigoris, Oceanus Procellarum, Mare Fecunditatis, Mare Nubium, and Mare Tranquilitatis), Noteably, wrinkle ridges in Oceanus Procellarum and Mare Frigoris traverse the mare with a variety of orientations implying a complex history of deformation [*Schultz et al.*, 2010; *Watters et al.*, 2010; 2012; *Banks et al.*, 2011; *Williams et al.*, 2012; 2014].

On Mercury, wrinkle ridges in the interior plains of the Caloris basin, also associated with a mascon, can be compared and contrasted with ridges in the northern smooth plains and Caloris basin exterior plains, both non-mascon regions on Mercury. This is analogous to the comparison of mascon basins and non-mascon regions on the Moon.

3.2 Wrinkle ridge mapping

The locations of wrinkle ridges on Mercury and the Moon were digitized using global mosaics in a Geographic Information Systems (GIS) environment. We mapped wrinkle ridges on Mercury using global mosaics (250 m/pix) consisting of Wide-angle Camera (WAC) and Narrow-angle Camera (NAC) monochrome images [*Hawkins et al.*, 2007]. Additional orbital images collected at large solar incidence angles ranging from ~65° to 88° from nadir provided optimum lighting conditions for identifying and mapping wrinkle ridges in Mercury's northern smooth plains [*Watters et al.*, 2013; 2015]. On the Moon, we mapped wrinkle ridges using primarily a LROC WAC 100 m/pixel global mosaic. LROC NACs provided additional high-resolution images, up to 0.5 m-scale panchromatic images over a combined 5-km swath, for detailed mapping of individual ridges [*Robinson et al.*, 2010]. On both Mercury and the Moon, we digitized continuous wrinkle ridge segments, which we defined as segments that appeared to be unbroken in plan view at the resolution of the mosaic. In cases of segmented wrinkle ridges, we digitized only the segment in which the relief was measured (see Auxiliary Material).

3.3 Relief measurements

Where possible, data from the MLA [*Smith et al.*, 2012; *Zuber et al.*, 2012] and LOLA [*Smith et al.*, 2010] were used to measure the maximum relief of wrinkle ridges on Mercury and the Moon, respectively. Profiles across wrinkle ridges were extracted from individual altimeter tracks where they traverse the ridges at orthogonal or near orthogonal angles (60° to 90° from strike) (Figure 5). Elevation data extracted directly from MLA and LOLA altimetry tracks is preferable because altimeter tracks (1) provide the densest and most accurate elevation profiles across features, (2) avoid the loss of accuracy that can occur with profiles extracted from gridded, interpolated datasets and (3) provide greater spatial resolution along track than many stereo image derived digital elevation models (Figure 6).

MLA returned altimetry data averaged over surface areas between 15 and 100 m in diameter, spaced on average ~400 m apart along the altimeter ground track, with radial precision of individual ranging measurements of less than 1 m [*Zuber et al.*, 2012]. Spacing between elevation data points is closer near the north pole and becomes more widely spaced at the equator because MESSENGER's orbit has highly eccentric, near-polar orbit with its periapsis at high northern latitudes. MLA tracks were available for a variety of orientations over the smooth plains in Mercury's high northern latitudes, allowing the relief of many wrinkle ridges to be measured (Figure 2A, Table S1).

LOLA transmits 5 beams, returning the mean elevation of a 5-m diameter spot from a 50-km altitude orbit. LOLA tracks are comprised of five parallel profiles, ~12 m apart, with individual observation points in each profile separated by ~56 m [*Smith et al.*, 2010]. LOLA ranging has a vertical precision of ±0.1 m. LRO's polar orbit enables the relief of only east-west trending wrinkle ridges, to be measured using LOLA tracks (Figure 3A, Table S2).

Where sufficient altimetry tracks transecting the ridges at appropriate angles were not available, we extracted elevation profiles perpendicular to the structure from gridded digital elevation models (DEMs). For wrinkle ridges in Mercury's northern smooth plains (north of ~40°N), we used a ~500 m/pixel DEM derived by interpolating elevation points from MLA tracks (n = 46). For wrinkle ridges south of ~40°N in the Caloris interior and exterior smooth plains, where MLA data points are widely spaced, we measured the relief from DEMs derived from stereo photogrammetry of MESSENGER orbital or flyby images with spatial resolutions from 500 m/pixel to ~2.7 km/pixel and with vertical precision ±135 m (n = 55) [*Oberst et al.*, 2010; *Preusker et al.*, 2011]. On the Moon, we measured the relief across wrinkle ridges that did not trend east-west by extracting elevations from a global 100 m/pixel DEM derived from stereo photogrammetric analysis of WAC images (n = 111). The LROC WAC stereo-derived DEM has a vertical precision of ±10 m [*Scholten et al.*, 2012].

For ridges on both Mercury and the Moon, we compared elevation data available and selected the highest resolution and most reliable data source to extract elevation measurements to calculate the greatest measurable relief for each wrinkle ridge (see Auxiliary Material). Relief was measured by taking the difference between the highest elevation on the profile and the elevation at the major inflection point on the vergent side of the ridge [*Watters*, 1988]. For wrinkle ridges located on regional slopes, relief was measured using detrended elevation profiles. Profiles were detrended by subtracting a least squares linear fit from the elevation data across the wrinkle ridge. Tables S1 and S2 show the greatest relief measured for each wrinkle ridge.

4. Results

The relief of wrinkle ridges measured on Mercury ranges from ~112 to 776 m with a mean relief of ~350 m (median = ~340 m, n = 150) (Figure 8A, Table 1). Measured wrinkle ridges on the Moon range in relief from ~47 to 678 m with a mean relief of ~198 m (median = ~168 m, n = 150). On average, wrinkle ridges on Mercury are ~2 times higher than those on the Moon (Table 1, Figure 8). The wrinkle ridge with the greatest relief on Mercury measured in this study is Schiaparelli Dorsum at 776 m. Schiaparelli Dorsum is located in in Odin Planitia within the Caloris exterior smooth plains (~69.51°, 2.14°). On the Moon by contrast, the largest relief wrinkle ridge we measured was Dorsa Mawson (~49.43°, -1.04°), which is 678 m tall and is located in Mare Fecundidatis. Four percent of the measured wrinkle ridges on Mercury have reliefs greater than 600 m, which is larger than all wrinkle ridges on the Moon except for Dorsa Mawson.

The lunar wrinkle ridges were sub-divided into elevation offset ridges and ridges exhibiting typical wrinkle ridge morphology with a broad arch and super imposed ridge (Figure 5). Figure 7 shows a comparison of profiles extracted across wrinkle ridges using altimetry tracks versus the digital elevation models. The relief measurements for each wrinkle ridge population are plotted as box and whisker plots in Figure 8 (Tables S1 and S2 list the relief and length for each wrinkle ridge measured for this analysis). Statistics comparing different wrinkle ridge populations on both Mercury and the Moon are shown in Tables 1 and 2.

Elevation offset ridges have significantly larger mean reliefs (~343 m) than wrinkle ridges in the mascon basins on the Moon (Mare Crisium, Serenitatis, Imbrium, and Humorum) as well as non-mascon basons Mare Frigoris and Oceanus Procellarum (Figure 8C). Although variations in the reliefs of wrinkle ridges for each lunar mare basin exist, there are no statistically significant differences between those in mascon and non-mascon environments.

The relief of wrinkle ridges on Mercury in the northern smooth plains and Caloris basin exterior plains (non-mascons) range in relief from 112 to 776 m (mean = 354 m) are similar to wrinkle ridges in the Caloris basin interior (mascon) that range from 153 to 567 m (mean = 335 m) (Figure 8B). When the wrinkle ridges of Caloris are divided into the interior and exterior smooth plains, there is still no statistically significant difference between the relief of wrinkle ridges in the Caloris exterior plains and those in the northern smooth plains compared to wrinkle ridges in the Caloris interior plains which are associated with a mascon (Figure 8C). The wrinkle ridges with the smallest relief occur near the center of the Caloris basin (Figure 3).

.

5. Discussion

Overall, the populations of wrinkle ridges on Mercury and the Moon have statistically significant differences in relief (Figure 8A). On Mercury, wrinkle ridges typically exhibit greater relief than wrinkle ridges on the Moon. This is true especially in the northern smooth plains and Caloris exterior plains where wrinkle ridge relief exceeds 600 m. We interpret the differences in relief between wrinkle ridges on the Moon and Mercury to reflect differences in the accumulated contractional strain of volcanic units on the two bodies.

The radius of Mercury is ~2,440 km, ~1.4 times larger than the Moon (radius = ~1,737.4 km). Globally distributed lobate scarps on Mercury and the Moon are believed to have formed primarily from horizontally isotropic compressional stresses resulting from global radial contraction [*Strom et al.*, 1975; *Solomon and Head*, 1979; *Solomon et al.*, 2008; *Watters and Nimmo*, 2010; *Watters et al.*, 1998, 2004, 2009c, 2010, 2015a, b]. The distribution of small-scale lunar lobate scarps, most with maximum reliefs <100 m and proportionally smaller lengths (less than tens of kilometers), indicate less than 100 m radial global contraction of the Moon [*Banks et al.*, 2012; *Watters and Johnston*, 2010; *Watters et al.*, 2010; *Watters et al.*, 2012a, 2015a]. Conservative estimates for the amount of global contraction from thrust faults on Mercury suggest a decrease in radius of no more than ~1 to 2 km [*Strom et al.*, 1975; *Watters*, 1988; *Watters et al.*, 1998; 2009c; 2013; *Watters and Anderson*, 2018], although some researchers estimates of the radius change are as high as ~3.6 to 7 km [*Di Achille et al.*, 2012; *Byrne et al.*, 2014]. Regardless, these estimates indicate that global contraction was at least an order of magnitude greater on Mercury than on the Moon.

We suggest that the existence of extremely large wrinkle ridges (>600 m) in the Caloris exterior smooth plains and the northern smooth plains may be due to the combination of compressional stresses from regional load-induced subsidence and global contraction (Figure 9). Wrinkle ridges in the Caloris interior are smaller in relief than those in the northern smooth plains or Caloris exterior plains. One possible explanation is that the impact event that formed the Caloris basin temporarily reset the regional stress field [*Freed et al.*, 2009]. As the depth and extent of the impact damage zone diminishes with increasing radial distance from the impact center [*Freed et al.*, 2009], much of the Caloris exterior plains may have been far enough away that the pre-existing stress field was not completely reset. Thus, the lower relief and basin concentric orientation of wrinkle ridges in the interior of the Caloris basin suggest the compressional stresses from load-induced subsidence that formed the wrinkle ridges in the interior plains of Caloris were isolated to some degree from the background global compressional stresses.

Relatively young, small-scale lobate scarps on the Moon indicate a small amount of recent global contraction (<100 m) [*Watters et al.*, 2010; 2015]. This suggests that compressional stresses from load-induced subsidence dominated in the formation of lunar wrinkle ridges and that there was little contribution from global contraction. Wrinkle ridges located in mascon basins (i.e. Serenitatis, Crisium, and Imbrium), although slightly larger in relief than wrinkle ridges in non-mascon regions (i.e. Procellarum and Frigoris), are not statistically significantly different, suggesting comparable levels of contractional strain in both mascon basins and non-mascon mare. These observations suggest that the presence of a mascon does not strongly influence the amount of subsidence and contraction of the mare basalt on the Moon or the smooth plains volcanics on Mercury. However, elevation offset ridges on the Moon are statistically significantly different than non-elevation offset ridges on the Moon. Since the majority of the elevation offset ridges we observed correlate with free-air positive anomalies of mascons, the increased relief observed in the elevation offset ridges may be explained by the excess mare basalt infill and that other factors such as post impact cooling and isostatic uplift expected in mascon tectonics [*Neumann et al*., 1996; *Melosh et al*., 2013] (Figure 10). However, several wrinkle ridges exist in mascons and do not exhibit statistically greater reliefs than those in non-mascons. This evidence that mascons do not host wrinkle ridges with greater structural relief may further indicate the critical role lithospheric thickness plays in supporting the mare loads by either allowing or inhibiting subsidence and contraction [see *Melosh*, 1978].

6. Conclusions

Results from morphometric analyses indicate that wrinkle ridges on Mercury are ~2 times higher in mean relief than wrinkle ridges on the Moon. Wrinkle ridges fall within an envelope ranging in relief from ~112 to 776 m on Mercury and ~47 to 678 m on the Moon. In general, a much greater contribution from global contraction is the most likely explanation for the greater relief of wrinkle ridges on Mercury compared to those on the Moon. The smaller relief of wrinkle ridges located in the Caloris interior plains relative to extremely large relief wrinkle ridges (>600 m) in the northern smooth plains and Caloris exterior plains may be the result of some degree of isolation of the Caloris interior from global contraction stresses due to impact damage. The observation that mascon basins do not host wrinkle ridges with greater structural relief relative to non-mascon units may indicate the critical role lithospheric thickness plays in subsidence and contraction of volcanic sequences on the Moon and Mercury.

ACKNOWLEDGEMENTS

Reviewers and editor. We thank the MESSENGER and LRO science teams, engineers, and technical support personnel who provided direct support for different aspects of this analysis. Funding for this project was provided by grant GRANT NUMBER HERE and the Smithsonian Institution Fellowship Office.

REFERENCES

Baldwin, R.B., 1965. A fundamental survey of the Moon, McGraw-Hill, New York, NY.

Baldwin, R.B., 1970. A new method of determining the depth of lava in lunar maria, Astronomical Society Pacific Publication, 82, 857-864.

Banks, M.E., Watters, T.R. Robinson, M.S. Bell III, J.F. Pritchard, M.E. Williams, N.R., Daud, K., 2011. The search for lunar lobate scarps using images from the Lunar Reconnaissance Orbiter, in Lunar and Planetary Science Conference XLII, edited, p. Abstract 2736.

Banks, M.E., Watters, T.R. Robinson, M.S. Tornabene, L.L. Tran, T. Ojha, L., Williams, N.R., 2012. Morphometric analysis of small-scale lobate scarps on the Moon using data from the Lunar Reconnaissance Orbiter, Journal of Geophysical Research-Planets, 117, 11, doi:10.1029/2011je003907.

Becker, K.J., Weller, L.A. Edmundson, K. Becker, T.L. Robinson, M.S. Enns, A.C. Solomon, S.C., 2012. Global Controlled Mosaic of Mercury from MESSENGER Orbital Images, paper presented at 43rd Lunar and Planetary Science Conference.

Bilham, R., King, G., 1989. The morphology of strike-slip faults: examples from the San Andreas Fault, California, Journal of Geophysical Research-Solid Earth and Planets, 94(B8), 10204-10216, doi:10.1029/JB094iB08p10204.

Boyce, J.M., 1976. Ages of flow units in the lunar nearside maria based on Lunar Orbiter IV photographs, paper presented at Proceedings of the Lunar and Planetary Science Conference, 7.

Byrne, P.K., Klimczak, C., Celal Sengor, A.M., Solomon, S.C., Watters, T.R., and Hauck, S.A., II, 2014. Mercury's global contraction much greater than earlier estimates, Nature Geoscience, 7, 301-307, doi:10.1038/ngeo2097.

De Hon, R.A., Waskom, J.D., 1976. Geologic structure of the eastern mare basins, Proceedings of the Lunar Science Conference, 7th, 2729-2746.

De Hon, R.A., 1979. Thickness of the western mare basalts, Proceedings of the Lunar and Planetary Science Conference, 10th, 2935-2955.

De Hon, R.A., 1980. Variations in morphology of 15-20 km lunar craters: Implications for a major subsurface discontinuity, Proceedings of the Lunar and Plaentary Science Conference, 11th, 2207-2219.

Denevi, B.W., Ernst, C.E., Meyer, H.M., Robinson, M.S., Murchie, S.L., Whitten, J.L., Head, J.W., Watters, T.R., Solomon, S.C., Ostrach, L.R., Chapman, C.R., Byrne, P.K., Klimczak, C., and Peplowski, P.N., 2013. The Distribution and Origin of Smooth Plains on Mercury, Journal of Geophysical Research - Planets, 11(5), 891-907, doi:10.1002/jgre.20075.

Di Achille, G., Popa, C. Massironi, M. Epifani, E.M. Zusi, M. Cremonese, G., Palumbo P., 2012, Mercury's radius change estimates revisited using MESSENGER data, Icarus, 221(1), 456-460, doi:10.1016/j.icarus.2012.07.005.

Egea-Gonzalez, I., Ruiz, J., Fernandez, C., Williams, J.P., Marquez, A., Lara, L.M., 2012. Depth of faulting and ancient heat flows in the Kuiper region of Mercury from lobate scarp topography, Planetary and Space Science, 60(1), 193-198, doi:10.1016/j.pss.2011.08.003.

Fassett, C. I., J.W. Head, D.T. Blewett, C.R. Chapman, J.L. Dickson, S.L. Murchie, S.C. Solomon, and T.R. Watters (2009), Caloris impact basin: Exterior geomorphology, stratigraphy, morphometry, radial sculpture, and smooth plains deposits, Earth and Planetary Science Letters, 285(3-4), 297-308, doi:10.1016/j.epsl.2009.05.022.

Fielder, G. (1961), Structure of the Moon's suface, Pergamon, New York, NY.

Freed, A.M., H.J. Melosh, and S.C. Solomon (2001), Tectonics of mascon loading: Resolution of the strike-slip faulting paradox, Journal of Geophysical Research-Planets, 106(E9), 20603-20620, doi:10.1029/2000je001347.

Freed, A.M., S.C. Solomon, T.R. Watters, R.J. Phillips, and M.T. Zuber (2009), Could Pantheon Fossae be the result of the Apollodorus crater-forming impact within the Caloris basin, Mercury?, Earth and Planetary Science Letters, 285(3-4), 320-327, doi:10.1016/j.epsl.2009.02.038.

Gilbert, G.K. (1893), The Moon's face, a study of the origin and its features, Philosophy Society of Washington Bulletin, 12, 241 - 292.

Golombek, M.P., F.S. Anderson, and M.T. Zuber (2001), Martian wrinkle ridge topography: Evidence for subsurface faults from MOLA, J. Geophys. Res., 106(E10), 23811-23821, doi:10.1029/2000JE001308.

Harmon, J.K., D.B. Campbell, D.L. Bindschadler, J.W. Head, and Shapiro, II (1986), Radar altimetry of Mercury - a preliminary analysis, Journal of Geophysical Research-Solid Earth and Planets, 91(B1), 385-401, doi:10.1029/JB091iB01p00385.

Hawkins, S.E., J.D. Boldt, Darlington, E.H., Espiritu, R.E. Gold, B. Gotwols, M.P. Grey, C.D. Hash, J.R. Hayes, S.E. Jaskulek, C.J. Kardian Jr., M.R. Keller, E.R. Malaret, S.L. Murchie, P.K. Murphy, K. Peacock, L.M. Prockter, R.A. Reiter, M.S. Robinson, E.D. Schaefer, R.G. Shelton, R.E. Sterner II, H.W. Taylor, T.R. Watters, and B.D. Williams, 2007. The Mercury Dual Imaging System on the MESSENGER spacecraft, Space Science Reviews, 131(1-4), 247-338, doi:10.1007/s11214-007-9266-3.

Head, J.W., C.R. Chapman, R.G. Strom, C.I. Fassett, B.W. Denevi, D.T. Blewett, C.M. Ernst, T.R. Watters, S.C. Solomon, S.L. Murchie, L.M. Procketer, N.L. Chabot, J.J. Gillis-

Davis, J.L. Whitten, T.A. Goudge, D.M.H. Baker, D.M. Hurwitz, L.R.Ostrach, Z. Xiao, W.J. Merline, L. Kerber, J.L. Dickson, J. Oberst, P.K. Byrne, C. Klimczak, and L.R. Nittler, 2011. Flood Volcanism in the Northern High Latitudes of Mercury Revealed by MESSENGER, Science, 333(6051), 1853-1856, doi:10.1126/science.1211997.

Head, J.W., S.L. Murchie, L.M. Procker, M.S. Robinson, S.C. Solomon, R.G. Strom, C.R. Chapman, T.R. Watters, W.E. McClintock, D.T. Blewett, and J.J. Gillis-Davis (2008), Volcanism on Mercury: Evidence from the first MESSENGER flyby, Science, 321(5885), 69-72, doi:10.1126/science.1159256.

Head, J.W., S.L. Murchie, L.M. Prockter, M.S. Robinson, S.C. Solomon, R.G. Strom, C.R. Chapman, T.R. Watters, W.E. McClintock, D.T. Blewett, and J.J. Gillis-Davis (2009), Volcanism on Mercury: Evidence from the first MESSENGER flyby for extrusive and explosive activity and the volcanic origin of plains, Earth and Planetary Science Letters, 285(3-4), 227-242, doi:10.1016/j.epsl.2009.03.007.

King, G., and M. Ellis (1990), The origin of large local uplift in extensional regions, Nature, 348(6303), 689-692, doi:10.1038/348689a0.

King, G.C.P., R.S. Stein, and J. Lin (1994), Static stress changes and the triggering of earthquakes, Bulletin of the Seismological Society of America, 84(3), 935-953.

King, G.C. P., R.S. Stein, and J.B. Rundle (1988), The growth of geological structures by repeated earthquakes. 1. Conceptual-Framework, Journal of Geophysical Research-Solid Earth and Planets, 93(B11), 13307-13318, doi:10.1029/JB093iB11p13307.

Klimczak, C., T.R. Watters, C.M. Ernst, A.M. Freed, P.K. Byrne, S.C. Solomon, D. M. Blair, and J.W. Head (2012), Deformation associated with ghost craters and basins in volcanic smooth plains on Mercury: Strain analysis and implications for plains evolution, Journal of Geophysical Research-Planets, 117, 15, doi:10.1029/2012je004100.

Klimczak, C., C.M. Ernst, P.K. Byrne, S.C. Solomon, T.R. Watters, S.L. Murchie, F.P., and J.A. Balcerski (2013), Insights into the subsurface structure of the Caloris basin, Mercury, from assessments of mechanical layering and changes in long-wavelength topography, Journal of Geophysical Research-Planets, 118, 2030-2044, doi:10.1002/jgre.20157.

Lin, J., and R.S. Stein (2004), Stress triggering in thrust and subduction earthquakes and stress interaction between the southern San Andreas and nearby thrust and strike-slip faults, J. Geophys. Res., 109(B2), B02303, doi:10.1029/2003JB002607.

Maxwell, T.A., F. El-Baz, and S.H. Ward (1975), Distribution, Morphology, and Origin of Ridges and Arches in Mare Serenitatis, Geological Society of America Bulletin, 86(9), 1273-1278.

Maxwell, T.A., and A.W. Gifford (1980), Ridge systems of Caloris: Comparison with lunar basins, paper presented at Lunar and Planetary Science Conference.

Melosh, H.J., and W.B. McKinnon (1988), The Tectonics of Mercury, in Mercury, edited, pp. 374-400, University of Arizona Press.

Melosh, H.J., A.M. Freed, B.C. Johnson, D. M. Blair, J.C. Andrews-Hanna, G.A. Neumann, R.J. Phillips, D.E. Smith, S.C. Solomon, M.A. Wieczorek, and M.T. Zuber (2013), The Origin of Lunar Mascon Basins, Science, 340(1552), doi:10.1126/science.1235768.

Neumann, G. A., M. T. Zuber, D. E. Smith, F. G. Lemoine, 1996. The lunar crust: Global structure and signature of major basins, Journal of Geophysical Research, 101, 16841–16863, doi:10.1029/96JE01246.

Nittler, L.R., Starr, R.D., Weider, S.Z., McCoy, T.J., Boynton, W.V., Ebel, D.S., Ernst, C.M., Evans, L.G., Goldsten, J.O., Hamara, D.K., Lawrence, D.J., McNutt, R.L., Jr., Schlemm, C.E., II, Solomon, S.C., Sprague, A.L., 2011. The Major-Element Composition of Mercury's Surface from MESSENGER X-ray Spectrometry, Science, 333.

Oberst, J., F. Preusker, R.J. Phillips, T.R. Watters, J.W. Head, M.T. Zuber, and S.C. Solomon (2010), The morphology of Mercury's Caloris basin as seen in MESSENGER stereo topographic models, Icarus, 209(1), 230-238, doi:10.1016/j.icarus.2010.03.009.

Okubo, C.H., and R.A. Schultz (2003), Two-dimensional wrinkle ridge strain & energy release based on numerical modeling of MOLA topography, paper presented at Proceedings of the Lunar and Planetary Science Conference.

Plescia, J.B., and M.P. Golombek (1986), Origin of planetary wrinkle ridges based on the study of terrestrial analogs, Geological Society of America Bulletin, 97(11), 1289-1299.

Preusker, F., J. Oberst, J.W. Head, T.R. Watters, M.S. Robinson, M.T. Zuber, and S.C. Solomon (2011), Stereo topographic models of Mercury after three MESSENGER flybys, Planetary and Space Science, 59(15), 1910-1917, doi:10.1016/j.pss.2011.07.005.

Robinson, M.S., S.M. Brylow, M. Tschimmel, D. Humm, S.J. Lawrence, P.C. Thomas, B.W. Denevi, E. Bowman-Cisneros, J. Zerr, M.A. Ravine, M.A. Caplinger, F.T. Ghaemi, J.A. Schaffner, M.C. Malin, P. Mahanti, A. Bartels, J. Anderson, T.N. Tran, E.M. Eliason, A.S. McEwen, E. Turtle, B.L. Jolliff, and H. Hiesinger (2010), Lunar Reconnaissance Orbiter Camera (LROC) Instrument Overview, Space Science Reviews, 150(1-4), 81-124, doi:10.1007/s11214-010-9634-2.

Scholten, F., J. Oberst, K.D. Matz, T. Roatsch, M. Wahlisch, E.J. Speyerer, and M.S. Robinson (2012), GLD100: The near-global lunar 100 m raster DTM from LROC WAC stereo image data, Journal of Geophysical Research-Planets, 117, doi:10.1029/2011je003926.

Schultz, R.A. (2000), Localization of bedding plane slip and backthrust faults above blind thrust faults: Keys to wrinkle ridge structure, J. Geophys. Res., 105(E5), 12035-12052, doi:10.1029/1999JE001212.

Schultz, R.A., E. Hauber, S.A. Kattenhorn, C.H. Okubo, and T.R. Watters (2010), Interpretation and analysis of planetary structures, Journal of Structural Geology, 32(6), 855-875, doi:10.1016/j.jsg.2009.09.005.

Schultz, R.A., C.H. Okubo, and S.J. Wilkins (2006), Displacement-length scaling relations for faults on the terrestrial planets, Journal of Structural Geology, 28(12), 2182-2193, doi:10.1016/j.jsg.2006.03.034.

Schultz, R.A., and T.R. Watters (2001), Forward mechanical modeling of the Amenthes Rupes thrust fault on Mars, Geophysical Research Letters, 28(24), 4659-4662, doi:10.1029/2001gl013468.

Smith, D.E., M.T. Zuber, G.B. Jackson, H. Riris, G.A. Neumann, X. Sun, J.F. McGarry, J.F. Cavanaugh, L.A. Ramos-Izquierdo, R. Zellar, M.H. Torrence, E. Mazarico, J. Connelly, A. Matuszeski, M. Ott, D.D. Rowlands, T. Zagwodzki, M.H. Torrence, R. Katz, I. Kleyner, C. Peters, P. Liiva, C. Coltharp, S. Schmidt, L. Ramsey, V.S. Scott, G. Unger, D.C. Krebs, A.D. Novo-Gradac, G.B. Shaw, and A.W. Yu (2010), The Lunar Orbiter Laser Altimeter Investigation on the Lunar Reconnaissance Orbiter Mission, Space Science Reviews, 150(1-4), 209-241, doi:10.1007/s11214-009-9512-y.

Smith, D.E., M.T. Zuber, R.J. Phillips, S.C. Solomon, S.A. Hauck II, F.G. Lemoine, E. Mazarico, G.A. Neumann, S.J. Peale, J. Margot, C.L. Johnson, M.H. Torrence, M.E. Perry, D.D. Rowlands, S. Goossens, J.W. Head, and A.H. Taylor (2012), Gravity Field and Internal Structure of Mercury from MESSENGER, Science, 336(6078), 214-217, doi:10.1126/science.1218809.

Solomon, S.C., and J.W. Head (1979), Vertical movement in mare basins - relation to mare emplacement, basin tectonics, and lunar thermal history, Journal of Geophysical Research, 84(NB4), 1667-1682, doi:10.1029/JB084iB04p01667.

Solomon, S.C., and J.W. Head (1980), Lunar mascon basins: Lava filling, tectonics, and evolution of the lithosphere, Reviews of Geophysics, 18(1), 107-141, doi:10.1029/RG018i001p00107.

Solomon, S.C., R.L. McNutt Jr., T.R. Watters, D.J. Lawrence, W.C. Feldman, J.W. Head, S.M. Krimigis, S.L. Murchie, R.J. Phillips, J.A. Slavin, and M.T. Zuber (2008), Return to Mercury: A global perspective on MESSENGER's first mercury flyby, Science, 321(5885), 59-62, doi:10.1126/science.1159706.

Stein, R.S., and G.C.P. King (1984), Seismic potential revealed by surface folding - 1983 Coalinga, California, Earthquake, Science, 224(4651), 869-872, doi:10.1126/science.224.4651.869.

Stein, R.S., G.C.P. King, and J.B. Rundle (1988), The growth of geological structures by repeated earthquakes. 2. Field examples of continental dip-slip faults, Journal of Geophysical Research-Solid Earth and Planets, 93(B11), 13319-13331, doi:10.1029/JB093iB11p13319.

Strom, R.G. (1970), Lunar mare ridges, rings, and volcanic ring complexes, Transactions-American Geophysical Union, 51(11), 773-&.

Strom, R.G., N.J. Trask, and J.E. Guest (1975), Tectonism and Volcanism on Mercury, J. Geophys. Res., 80(17), 2478-2507, doi:10.1029/JB080i017p02478.

Suppe, J., and C. Connors (1992), Critial taper erdge mechanics of fold-and-thrust belts on Venus - initial results from MAGELLAN, Journal of Geophysical Research-Planets, 97(E8), 13545-13561.

Taboada, A., J.C. Bousquet, and H. Philip (1993), Coseismic elastic models of folds above blind thrusts in the Betic Cordilleras (Spain) and evaluation of seismic hazard, Tectonophysics, 220(1-4), 223-241, doi:10.1016/0040-1951(93)90233-a.

Toda, S., R.S. Stein, K. Richards-Dinger, and S.B. Bozkurt (2005), Forecasting the evolution of seismicity in southern California: Animations built on earthquake stress transfer, Journal of Geophysical Research, 110(B5), B05S16, doi:10.1029/2004JB003415, 200.

Watters, T.R. (1988), Wrinkle Ridge Assemblages on the Terrestrial Planets, J. Geophys. Res., 93(B9), 10236-10254, doi:10.1029/JB093iB09p10236.

Watters, T.R. (1991), Origin of periodically spaced wrinkle ridges on the Tharsis Plateau of Mars, Journal of Geophysical Research-Planets, 96(E1), 15599-15616, doi:10.1029/91je01402.

Watters, T.R., M.S. Robinson, and A. C. Cook (1998), Topography of lobate scarps on Mercury: New constraints on the planet's contraction, Geology, 26(11), 991-994, doi:10.1130/0091-7613(1998)026<0991:tolsom>2.3.co;2.

Watters, T.R., R.A. Schultz, M. S. Robinson, and A. C. Cook (2002), The mechanical and thermal structure of Mercury's early lithosphere, Geophysical Research Letters, 29(11), 4, doi:10.1029/2001gl014308.

Watters, T.R. (2004), Elastic dislocation modeling of wrinkle ridges on Mars, Icarus, 171(2), 284-294, doi:10.1016/j.icarus.2004.05.024.

Watters, T.R., M.S. Robinson, C.R. Bina, and P.D. Spudis (2004), Thrust faults and the global contraction of Mercury, Geophysical Research Letters, 31(4), 5, doi:10.1029/2003gl019171.

Watters, T.R., F. Nimmo, and M.S. Robinson (2005), Extensional troughs in the Caloris basin of Mercury: Evidence of lateral crustal flow, Geology, 33(8), 669-672, doi:10.1130/g21678.

Watters, T.R., J.W. Head, S.C. Solomon, M.S. Robinson, C.R. Chapman, B.W. Denevi, C.I. Fassett, S.L. Murchie, and R.G. Strom (2009a), Evolution of the Rembrandt Impact Basin on Mercury, Science, 324(5927), 618-621, doi:10.1126/science.1172109.

Watters, T.R., S.L. Murchie, M.S. Robinson, S.C. Solomon, B.W. Denevi, S.L. Andre, and J.W. Head (2009b), Emplacement and tectonic deformation of smooth plains in the Caloris basin, Mercury, Earth and Planetary Science Letters, 285(3-4), 309-319, doi:10.1016/j.epsl.2009.03.040.

Watters, T.R., S.C. Solomon, M.S. Robinson, J.W. Head, S.L. Andre, S.A. Hauck, and S.L. Murchie (2009c), The tectonics of Mercury: The view after MESSENGER'S first flyby, Earth and Planetary Science Letters, 285(3-4), 283-296, doi:10.1016/j.epsl.2009.01.025.

Watters, T., and C. Johnston (2010), Lunar Tectonics, in Planetary Tectonics, edited by T. R. Watters and R. A. Schultz, pp. 121-182, Cambridge University Press, New York, NY.

Watters, T.R., and F. Nimmo (2010), The tectonics of Mercury, in Planetary Tectonics, edited by T.R. Watters and R. A. Schultz, pp. 15-80, Cambridge University Press, New York.

Watters, T.R., M.S. Robinson, R.A. Beyer, M.E. Banks, J.F. Bell III, M.E. Pritchard, H. Hiesinger, C.H. van der Bogert, P.C. Thomas, E.P. Turtle, and N.R. Williams (2010), Evidence of Recent Thrust Faulting on the Moon Revealed by the Lunar Reconnaissance Orbiter Camera, Science, 329(5994), 936-940, doi:10.1126/science.1189590.

Watters, T.R., and R.A. Schultz (2010), Planetary tectonics: introduction, in Planetary Tectonics, edited by T. R. Watters and R. A. Schultz, pp. 15-80, Cambridge University Press, New York.

Watters, T.R., P.K. Byrne, C. Klimczak, A.C. Enns, M.E. Banks, L.S. Walsh, C.M. Ernst, M.S. Robinson, J.J. Gillis-Davis, S.C. Solomon, R.S. Strom, and K. Gwinner (2011a), The Tectonics of Mercury: The View from Orbit, in American Geophysical Union, edited.

Watters, T.R., P.C. Thomas, and M.S. Robinson (2011b), Thrust faults and the near-surface strength of asteroid 433 Eros, Geophysical Research Letters, 38, 5, doi:10.1029/2010gl045302.

Watters, T.R., S.C. Solomon, C. Klimczak, A.M. Freed, J.W. Head, C.M. Ernst, D.M. Blair, T.A. Goudge, and P.K. Byrne (2012a), Extension and contraction within volcanically buried impact craters and basins on Mercury, Geology, 40(12), 1123-1126.

Watters, T.R., M.S. Robinson, M.E. Banks, T. Tran, and B. Denevi (2012b), Recent extensional tectonics on the Moon revealed by the Lunar Reconnaissance Orbiter Camera, Nature Geoscience, doi:10.1038/ngeo1387.

Watters, T.R., S.C. Solomon, C. Klimczak, M.M. Selvans, L.S. Walsh, M.E. Banks, P.K. Byrne, B.W. Denevi, C.M. Ernst, S.L. Murchie, J. Oberst, F. Preusker, S.A. Hauck, II, M.T.

Zuber, and R.J. Phillips (2013), Distribution of prominent lobate scarps on Mercury: Contribution to global radial contraction, Lunar and Planetary Science Conference, Houston, TX, Abstract #2213.

Watters, T.R., Anderson, S.E., 2018, The tectonics of Mercury: A post MESSENGER view, Lunar and Planetary Science Conference, Houston, TX, Abstract #2083.

Watters, T.R., DeFelice, D.R., 2018, Wrinkle ridges and ancient rifts bordering Procellarum and Frigoris idenfied in GRAIL gravity data, Lunar and Planetary Science Conference, Houston, TX, Abstract #2044.

Wells, D. L., and K.J. Coppersmith (1994), New empirical relationships among magnitude, rupture length, rupture width, rupture area, and surface displacement, Bulletin of the Seismological Society of America, 84(4), 974-1002.

Wilhelms, D.E. (1987), The Geologic History of the Moon, U.S. Government Printing Office, Washington, DC.

Wilhelms, D.E., and J.F. McCauley (1971), Geologic map of the nearside of the Moon.

Williams, N.R., J.F.I. Bell, T.R. Watters, M.E. Banks, and M.S. Robinson (2012), Tectonic mapping of mare frigoris using lunar reconnaissance orbiter camera images, paper presented at 43rd Lunar and Planetary Science Conference.

Williams, N.R., T.R. Watters, M.E. Pritchard, M.E. Banks, and J.F. Bell (2013), Fault dislocation modeled structure of lobate scarps from Lunar Reconnaissance Orbiter Camera digital terrain models, Journal of Geophysical Research: Planets, 118, 224-233, doi:10.1002/jgre.20051.

Williams, N.R., J.F. Bell III, T.R. Watters, M.E. Banks, and M.S. Robinson (2014), Timing and controls of tectonic deformation in Mare Frigoris, paper presented at 45th Lunar and Planetary Science Conference.

Zuber, M.T., D.E. Smith, R.J. Phillips, S.C. Solomon, G.A. Neumann, S.A. Hauck, II, S.J. Peale, O.S. Barnouin, J.W. Head, C.L. Johnson, F.G. Lemoine, E. Mazarico, X. Sun, M.H. Torrence, A.M. Freed, C. Klimczak, J. Margot, J. Oberst, M.E. Perry, R.L. McNutt, Jr., J.A. Balcerski, N. Michel, M. Talpe, and D. Yang (2012), Topography of the Northern Hemisphere of Mercury from MESSENGER Laser Altimetry, Science, 336(6078), 217-220, doi:10.1126/science.1218805.

Zuber, M. T., D.E. Smith, M.M. Watkins, S.W. Asmar, A.S. Konopliv, F.G. Lemoine, H.J. Melosh, G.A.Neumann, R.J. Phillips, S.C. Solomon, M.A. Wieczorek, J.G. Williams, S.J. Goossens, G. Kruizinga, E. Mazarico, R.S. Park, D.N. Yuan (2013), Gravity Field of the Moon from the Gravity Recovery and Interior Laboratory (GRAIL) Mission, Science, 339(6120), 668-671, doi:10.1126/science.1231507.

TABLES

Table 1. General comparison of wrinkle ridge reliefs (m) on the Moon and Mercury

Location		Minimum	5%	25%	Median	Mean	75%	95%	Maximum	Number
The Moon	All measured wrinkle ridges on the Moon	47	68	116	168	198	256	411	678	150
	All measured wrinkle ridges on the Moon with elevation offset ridges removed	47	65	113	156	181	232	353	678	134
	Wrinkle ridges located in lunar mascons	47	80	127	206	220	283	429	563	72
	Wrinkle ridges located in lunar non-mascons	52	63	116	155	179	210	357	357	84
Mercury	All measured wrinkle ridges on Mercury	112	160	245	340	350	437	593	776	150
	Wrinkle ridges located in the Caloris basin interior plains (mascon)	153	188	248	318	335	422	545	567	31
	Wrinkle ridges in northern smooth plains and Caloris basin exterior plains(non-mascons)	112	155	246	344	354	444	600	776	119
Ratio	Ratio Mercury/Moon reliefs for all measured ridges	3.11	2.47	2.16	2.12	1.86	1.82	1.46	1.32	

Table 2. Detailed comparison of wrinkle ridge reliefs (m) on the Moon and Mercury

Location			Minimum	5%	25%	Median	Mean	75%	95%	Maximum	Number
The Moon	*mascons*	Mare Crisium	47	66	99	153	175	234	330	420	12
		Mare Serenitatis	84	89	124	172	187	248	305	344	24
		Mare Imbrium	76	76	134	190	217	281	427	432	18
		Mare Humorum	117	119	126	134	161	184	223	233	3
		mascons with elevation offset ridges removed	47	80	113	171	193	257	386	432	57
	non-mascons	Mare Frigoris	57	59	70	126	155	204	312	391	17
		Oceanus Procellarum	52	73	119	151	159	193	270	358	53
		Mare Fecunditatis	343	360	427	511	511	594	661	678	2
		Mare Nubium	115	126	170	224	213	262	292	300	3
		Mare Tranquillitatis	144	154	196	248	248	299	341	351	2
		non-mascons with elevation offset ridges removed	52	63	114	150	172	205	345	678	77
	elevation offset ridges	All	79	152	256	336	343	411	581	636	16
Mercury	*mascons*	Caloris Basin's interior	153	188	248	318	335	422	545	567	31
	mascons and non-mascons	Caloris Basin Region (interior and exterior plains)	141	177	242	337	350	447	567	634	52
	non-mascons	Circum-Caloris Plains	141	167	237	383	373	467	574	634	21
		Northern Smooth Plains	112	155	250	340	350	420	602	776	98

FIGURE CAPTIONS

Figure 1. Free-air gravity and tectonics of Mercury (A) and the Moon (B) on a Mollweide equal area projection of a shaded relief map merged with a global MDIS or LROC WAC monochrome mosaic. Positive gravity anomalies correspond to mascon basin environments. The gravity model from Mercury is from radio tracking of the MESSENGER spacecraft [*Smith et al.*, 2012]. Lunar gravity model is from the Gravity Recovery and Interior Laboratory (GRAIL) spacecraft gravity model [*Zuber et al.*, 2013]. Tectonic features are wrinkle ridges (white) we digitized for this study. Mercury smooth plains boundary from Denevi et al. [2012] and mare basins boundary digitized by Steven Koeber.

Figure 2. Locations of wrinkle ridges in the northern smooth plains of Mercury measured for this study (stars, see Table S1). Stars are colored based on their measured relief. Wrinkle ridges are plotted on a north polar projection of combined 250 m/pixel high-incidence angle and 500 m/pixel monochrome global mosaics of MDIS images overlaid with a (A) DEM created from MLA tracks [*Zuber et al.*, 2012] and (B) the gravity model from Mercury from radio tracking of the MESSENGER spacecraft [*Smith et al.*, 2012].

Figure 3. Locations of wrinkle ridges in the Caloris basin region of Mercury measured for this study (stars, see Table S1). Stars are colored based on their measured relief. Smooth plains boundary from Denevi et al. [2012]. Wrinkle ridges are plotted on a Equirectangular projection of the MDIS mosaic overlaid with a (A) stereo derived DEM created from M1 Flyby imagery (1 km^2) [*Oberst et al.*, 2010; *Preusker et al.*, 2011], a stereo derived DEM created from orbital

imagery created by DLR (~500 m^2), and the USGS DEM (~2.7 km^2) [*Becker et al.*, 2012] and (B) the gravity model from Mercury from radio tracking of the MESSENGER spacecraft [*Smith et al.*, 2012]. The transparency of the elevation DEMs is set to 70%, therefore brighter colors in Map A indicate locations where DEM sources overlap.

Figure 4. Locations of 150 wrinkle ridges in the mare basins of the Moon that we measured for this study (stars, see Table S2) plotted on a 1:125,000,000 Equirectangular projection of a 100 m/pixel monochrome global mosaic of 400 m/pixel WAC images overlaid with a (A) global LROC WAC stereo derived DEM [*Scholten et al*., 2012] and (B) the lunar gravity model from the Gravity Recovery and Interior Laboratory (GRAIL) spacecraft gravity model [*Zuber et al.*, 2013]. Red boxes mark elevation offset wrinkle ridges. Stars are colored based on their measured relief. Mare basin boundaries were digitized by Steven Koeber.

Figure 5. A) Concentric wrinkle ridges in Mare Serenitatis, a mascon-basin environment where wrinkle ridge formation is attributed to subsidence. The LROC WAC stereo DEM has been clipped to the basin boundary to highlight the topography within the basin. Map scale is 1:20,000,000. Red boxes mark elevation offset wrinkle ridges. B) LOLA tracks and elevations overlaid on a WAC image of an elevation offset wrinkle ridge in southwestern Mare Serenitatis. LOLA elevation data were acquired using the Lunar Orbital Data Explorer (http://ode.rsl.wustl.edu). The topographic step shown in this profile is typical of elevation offset ridges [*Watters and DeFelice*, 2018]. In contrast, Figures 5 illustrates typical profiles for

wrinkle ridges on Mercury and the Moon that include a broad arch and superimposed ridge morphology.

Figure 6. Cross-section from altimetry tracks and imagery examples of wrinkle ridge from Mare Frigoris on the Moon (A) and in the northern smooth plains of Mercury (B) that show the typical wrinkle ridge broad arch and superimposed ridge morphology. The 1:1 scale cross-section of the mercurian wrinkle ridge (C) demonstrates that in reality changes in topography across wrinkle ridges are subtle. The inset zooms into the vergent side of the ridge used in the relief measurement where the largest change in relief corresponds to a slope of only 10°.

Figure 7. Comparison of elevation profiles extracted across wrinkle ridges from different elevation data sources for the Moon (A) and Mercury (B). We used LOLA tracks to measure the relief of nearly east-west trending lunar wrinkle ridges and the WAC stereo derived DEM to measure all other lunar wrinkle ridges. We selected the elevation data source for wrinkle ridges on Mercury depending on the highest resolution and coverage available for its location.

Figure 8. Box and whisker plots showing the relief of wrinkle ridge populations in the following regions: A) the Moon and Mercury, B) mascon and non-mascon basin environments, C) specified location. The box represents the interquartile range (which represents the middle 50% of the data). The vertical ends of the box are the 25th and 75th percentiles, the whiskers extend to the 95% of the data, and the X symbols represent outliers. Mean values are shown as diamonds and the median values as horizontal lines. Lunar elevation offset ridges are removed from A and B and locations in C, but are shown as a single population in C.

Figure 9. If the amount of subsidence induced contraction is comparable for basalt-like smooth plains on Mercury and mare basalts, it is expected that wrinkle ridges on the two bodies would have roughly similar structural relief. The large-relief wrinkle ridges in the northern smooth plains on Mercury and in the Caloris exterior plains are likely due to a combination of subsidence and global contraction (blue line) [Modified after *Watters*, 2004].

Figure 10. Wrinkle ridge rings (Figure 5) are interpreted to have been generated by mascon or basin-localized tectonics. The processes of mascon tectonics involve the occurrence of a large basin forming impact, followed by flood volcanism and then subsidence driven by loading resulting in contraction of the mare basalts. Lithospheric thickness in mascon and non-mascon regions likely plays a major role in controlling the amount of subsidence and contractional deformation. The upper map and cross-sections show a comparison of the free-air gravity anomaly and topographic profiles for a mascon compared to a non-mascon on the Moon. Although a greater gravity anomaly, and thus larger relief wrinkle ridges, are expected in Mare Serenitatis due to additional loading on the lithosphere, no statistical difference in wrinkle ridge relief is evident compared to the relief of wrinkle ridges in non-mascons. The lower diagram shows differences in deformation expected from stresses generated by mascon, or basin localized, tectonics [modified after *Solomon et al*., 1980)] compared to non-mascon regions. A difference in lithospheric thickness may be responsible for comparable amounts of contractional deformation in mascon and non-mascon settings.

Auxiliary Material for

Wrinkle ridges on Mercury and the Moon within and outside of mascons

Lisa S. Schleicher

(Center for Earth and Planetary Studies, National Air and Space Museum, Smithsonian Institution, Washington, DC 20560, USA)

Thomas R. Watters

(Center for Earth and Planetary Studies, National Air and Space Museum, Smithsonian Institution, Washington, DC 20560, USA)

Aaron J. Martin

(División de Geociencias Aplicadas, IPICYT, San Luis Potosí, México)

Maria E. Banks

(Center for Earth and Planetary Studies, National Air and Space Museum, Smithsonian Institution, Washington, DC 20560, USA)

(NASA Goddard Space Flight Center, Greenbelt, MD 20771, USA)

Icarus, 2018

Introduction

This dataset contains tables listing all wrinkle ridge relief measurements ("ts01.txt" and "ts02.txt") and a discussion of measurement uncertainty associated with imagery resolution and elevation data source as associated graphs ("text01.txt" and "fs03.eps"). GIS shapefiles for the wrinkle ridges digitized for this study are available by request to the authors.

2. ts01.txt, Mercurian wrinkle ridge locations and relief measurements

2.1 Column "Mercurian wrinkle ridge ID (informal)," text, Wrinkle ridges are unofficially named for the purposes of this study using abbreviations based on their specified geographic locations: NSP = northern smooth plains, NCCP = northern Caloris exterior plains, SCCP = southern Caloris exterior plains, and CB = Caloris basin interior. †Wrinkle ridges previously identified from Mariner 10 and MESSENGER flyby imagery [Watters et al., 2009c].

2.2 Column "Longitude," degrees, longitude (degrees east), on a -180 to 0 to +180 scale, of location of wrinkle ridge.

2.3 Column "Latitude," degrees, latitude of location of wrinkle ridge, north of equator.

2.4 Column "Relief," meters, maximum measurable relief at location of wrinkle ridge.

2.5 Column, "Topographic data source," text, source of elevation data used for relief measurement.

3. ts02.txt, Lunar wrinkle ridge locations and relief measurements

3.1 Column "Lunar wrinkle ridge ID (informal)," text, Wrinkle ridges are unofficially named for the purposes of this study using abbreviations based on specified geographic locations: CR = Mare Crisium, S = Mare Serenitatis, OP = Oceanus Procellarum, FR = Mare Frigoris, T =Mare Tranquillitatis, H = Mare Humorum, C = Mare Cognitum, NU = Mare Nubium, O = Mare

Orientale, FE = Mare Fecunditatis, SM = Mare Smythii, GC = Grimaldi Crater, KAC = Karrer Crater, KUC = Kugler Crater, and V = Vitello Crater. †Wrinkle ridge – lobate scarp transitions

3.2 Column “Longitude,” degrees, longitude (degrees east), on a -180 to 0 to +180 scale, of location of wrinkle ridge.

3.3 Column “Latitude,” degrees, latitude of location of wrinkle ridge, north of equator.

3.4 Column “Relief,” meters, maximum measurable relief at location of wrinkle ridge.

3.5 Column, “Topographic data source,” text, source of elevation data used for relief measurement.

4. text01.pdf, Document S1, resolution of imagery and elevation data sources and resulting uncertainty on wrinkle ridge mapping and relief measurements

5. ts03.txt, Relief measurement uncertainties from different elevation data sources

5.1 Column, "Location," text, planetary body, either Mercury or the Moon.

5.2 Column, "Source," elevation data source.

5.3 Column, "n," number of measurements.

5.4 Column, “Vertical precision,” meters, precision of elevation measurement from altimeter or digital elevation model.

5.5 Column, "Relief uncertainty," meters, uncertainty of relief measurement (2X vertical precision).

Document S1

Resolution of imagery and elevation data sources and resulting uncertainty on wrinkle ridge mapping and relief measurements

The varying imagery and elevation data sources available from MESSENGER and LRO for Mercury and the Moon solicit concern for any influence these different data sources may have on the relief and length measurements and ultimately the comparison of wrinkle ridge reliefs presented in this analysis (Table S3). Therefore, here we detail the influence of imagery resolution on mapping wrinkle ridges as well as use of varying elevation data sources on our relief measurements.

1. Mapping wrinkle ridges from different resolution global mosaics

Wrinkle ridges were digitized in GIS environment from either the 100 m/pixel LROC WAC for wrinkle ridges on the Moon or the 250 m/pixel MDIS imagery mosaic for wrinkle ridges on Mercury. Because the global mosaic for the Moon is ~2.5 times higher in resolution than the global mosaic for Mercury, some very small scale wrinkle ridges (<1 km) can be observed on the Moon and not on Mercury. We used a 500 m/pixel LROC WAC global mosaic in addition to the 100 m/pixel LROC WAC global mosaic when identifying and then digitizing digitize wrinkle ridges on the Moon. The majority of wrinkle ridges we digitized on the Moon are visible in both the 500 m/pixel and 100 m/pixel LROC WAC global mosaics. The 100 m/pixel global mosaic allowed the shape of the wrinkle ridge in map view to be more accurately mapped and whether the wrinkle ridge was continuous or segmented to be discerned.

2. Relief measurements from different elevation data sources

The relief of wrinkle ridges on Mercury were measured from MLA altimetry tracks (n = 46), MLA DEM (n = 58) and Flyby and orbital stereo-derived DEMs (n = 32). Relief across lunar wrinkle ridges was measured using either LOLA altimetry tracks (n = 33) or the WAC stereo-derived DEM (n = 117). The uncertainty associated with elevation measurements that comprise these elevation data sources is shown in Table S3. Since measuring the relief requires subtraction of two elevation data points, uncertainty associated with the elevation measurements is doubled. Therefore, the uncertainty associated with relief measurements is twice that of the elevation data used. For example, elevation data points comprising LOLA altimetry tracks have a vertical precision of ±10 cm. Therefore, the uncertainty associated with measuring the relief of a wrinkle ridge doubles to ±20 cm.

Altimetry tracks (LOLA or MLA) provided the most detailed view of wrinkle ridges in cross-section and the smallest uncertainty in vertical precision. Since the vertical precision is ±10 cm for LOLA and ±1 m for MLA, the uncertainty associated with relief measurements for wrinkle ridges measured using LOLA or MLA altimetry tracks or the MLA DEM is at least smaller than ~25 m in the relief dimension. The vertical precision of the WAC stereo-derived DEM is also quite small, only ±10 m. Therefore the uncertainty accompanying relief measurements from the WAC stereo derived DEM is smaller than ± 20 m.

Elevation data comprising the MESSENGER flyby and orbital stereo-derived DEMs has a vertical precision of ±135 m (±270 m in relief). Note however, that these are the worst case uncertainties and that in some cases profiles extracted across wrinkle ridges visible in the imagery did not exhibit any measurable reliefs. The stereo-derived DEMs uses MLA elevation data as control points when possible to help reduce the uncertainty associated with these elevation datasets. Since we cannot avoid these large uncertainties, we chose to regard measurements from the MESSENGER stereo-derived DEMs with caution when making our interpretations.

3. Greatest measurable relief

We report the greatest relief measured for each wrinkle ridge, however we note that this is not necessarily the maximum relief as MLA and LOLA profiles do not always provide continuous coverage across the entire length of each wrinkle ridge. When measuring relief from DEMs, it is possible to extract profiles across the entire length of the wrinkle ridge, which allowed the maximum relief to be determined. The relief measured from MLA or LOLA profiles is considered to be the “greatest measured relief” while relief measured from DEMs is considered to be the “maximum relief”.

References

Becker, K.J., Weller, L.A., Edmundson, K., Becker, T.L., Robinson, M.S., Enns, A.C., and Solomon, S.C.,2012. Global Controlled Mosaic of Mercury from MESSENGER Orbital Images, paper presented at 43rd Lunar and Planetary Science Conference.

Oberst, J., Preusker, F., Phillips, R.J., Watters, T.R., Head, J.W., Zuber, M.T., and Solomon S.C., 2010. The morphology of Mercury's Caloris basin as seen in MESSENGER stereo topographic models, Icarus, 209(1), 230-238, doi:10.1016/j.icarus.2010.03.009.

Preusker, F., Oberst, J., Head, J.W., Watters, T.R., Robinson, M.S., Zuber, M.T., and Solomon, S.C., 2011. Stereo topographic models of Mercury after three MESSENGER flybys, Planetary and Space Science, 59(15), 1910-1917, doi:10.1016/j.pss.2011.07.005.

Watters, T.R., Solomon, S.C., Robinson, M.S., Head, J.W., Andre, S.L., Hauck, S.A., and Murchie S.L., 2009c. The tectonics of Mercury: The view after MESSENGER'S first flyby, Earth and Planetary Science Letters, 285(3-4), 283-296, doi:10.1016/j.epsl.2009.01.025.

Zuber, M.T., Smith, D.E., Phillips, R.J., Solomon, S.C., Neumann, G.A., Hauck, S.A., Peale, S.J., Barnouin, O.S., Head, J.W., Johnson, C.L., Lemoine, F.G., Mazarico, E., Sun, X., Torrence, M.H., Freed, A.M., Klimczak, C., Margot, J., Oberst, J., Perry, M.E., McNutt, R.L. Jr., Balcerski, J.A., Michel, N., Talpe, M., and Yang, D., 2012. Topography of the Northern Hemisphere of Mercury from MESSENGER Laser Altimetry, Science, 336(6078), 217-220, doi:10.1126/science.1218805.

Table S1. Mercurian wrinkle ridge locations and relief measurements

Mercurian wrinkle ridge ID (informal)[a]	Longitude (°E)	Latitude (°N)	Relief (m)	Topographic data source
M-NSP1	27.15	62.54	352	MLA altimetry track
M-NSP2	-70.84	71.12	257	MLA altimetry track
M-NSP3	-76.07	73.26	343	MLA altimetry track
M-NSP4	113.18	78.95	390	MLA altimetry track
M-NSP5†	-43.49	73.59	622	MLA DEM
M-NSP6	134.45	75.10	547	MLA altimetry track
M-NSP7	-32.20	68.14	510	MLA altimetry track
M-NSP8	64.84	82.11	508	MLA altimetry track
M-NSP9	1.08	57.71	640	MLA DEM
M-NSP10	24.09	55.03	537	MLA altimetry track
M-NSP11	89.74	74.13	280	MLA altimetry track
M-NSP12	-95.55	69.73	152	MLA DEM
M-NSP13	14.38	80.76	384	MLA altimetry track
M-NSP14	88.74	78.18	593	MLA altimetry track
M-NSP15	76.73	65.57	379	MLA altimetry track
M-NSP16	35.12	65.86	387	MLA altimetry track
M-NSP17	-4.13	74.04	435	MLA altimetry track
M-NSP18	-25.64	63.13	551	MLA altimetry track
M-NSP19	51.15	64.33	304	MLA altimetry track
M-NSP20	68.91	59.48	282	MLA altimetry track
M-NSP21	-97.61	78.22	679.5	MLA altimetry track
M-NSP22	-15.59	57.16	344	MLA altimetry track
M-NSP23	39.04	62.04	312	MLA altimetry track
M-NSP24	24.06	57.13	352	MLA DEM
M-NSP25	-30.86	75.21	598	MLA DEM
M-NSP26	-17.84	78.87	484	MLA altimetry track
M-NSP27	-31.84	82.01	193	MLA DEM
M-NSP28	-74.11	66.39	458	MLA altimetry track
M-NSP29	29.53	77.62	371	MLA altimetry track
M-NSP30	-90.00	66.89	276	MLA DEM
M-NSP31	126.35	73.27	273	MLA altimetry track
M-NSP-32	3.03	82.15	257	MLA DEM
M-NSP33	54.63	79.74	217	MLA altimetry track
M-NSP34	53.99	77.24	175	MLA altimetry track
M-NSP35	42.61	70.53	314	MLA DEM
M-NSP36	51.99	67.31	223	MLA altimetry track
M-NSP37	30.16	81.49	230	MLA DEM
M-NSP38	-5.35	83.28	298	MLA altimetry track
M-NSP39	32.36	52.28	187	MLA DEM
M-NSP40	-28.17	55.93	391	MLA DEM
M-NSP41	41.95	56.49	318	MLA DEM

M-NSP42	44.87	55.11	426	MLA DEM
M-NSP43	-38.54	75.01	306	MLA DEM
M-NSP-44	42.03	58.14	352	MLA DEM
M-NSP45	6.31	34.97	149	M2 DEM flyby
M-NSP46	10.71	37.41	367	M2 DEM flyby
M-NSP47	-0.75	38.41	345	M2 DEM flyby
M-NSP48	10.74	51.24	404	MLA DEM
M-NSP49	-1.98	55.51	366	MLA DEM
M-NSP50	6.20	61.55	116	MLA DEM
M-NSP51	-3.66	54.45	369.5	MLA DEM
M-NSP52	77.70	1.05	382	M3 DEM flyby
M-NSP53	77.18	6.98	347	M3 DEM flyby
M-NSP54	76.88	4.49	475	M3 DEM flyby
M-NSP55	68.16	7.09	655.5	MLA altimetry track
M-NSP56	69.51	2.14	776	MLA altimetry track - Oblique Traverse
M-NSP57	113.49	77.89	489	MLA altimetry track
M-NSP58	113.76	75.65	415	MLA altimetry track
M-NSP59	-93.82	79.92	224	MLA altimetry track
M-NSP60	-100.81	73.94	421	MLA DEM
M-NSP61	-70.34	67.44	170	MLA altimetry track
M-NSP62	-86.17	74.99	331	MLA altimetry track
M-NSP63	37.70	46.53	180	MLA DEM
M-NSP64	43.57	41.48	473	MLA DEM
M-NSP65	41.27	40.23	232	MLA altimetry track
M-NSP66	41.70	44.68	238	MLA altimetry track
M-NSP67	39.79	50.06	249	MLA DEM
M-NSP68	46.39	60.05	237	MLA altimetry track
M-NSP69	-69.99	72.35	189	MLA altimetry track
M-NSP70	-79.77	71.47	287	MLA altimetry track
M-NSP71	29.33	67.13	201	MLA altimetry track
M-NSP72	134.89	71.18	464	MLA DEM
M-NSP73	39.32	66.44	326	MLA DEM
M-NSP74	5.70	76.27	252	MLA DEM
M-NSP75	-10.29	78.60	350	MLA altimetry track
M-NSP76	-26.94	68.82	239	MLA DEM
M-NSP77	-22.64	70.00	112	MLA DEM
M-NSP78	-11.40	71.57	418	MLA DEM
M-NSP79	-43.96	72.12	544	MLA DEM
M-NSP80	-35.15	67.52	358	MLA DEM
M-NSP81	50.36	58.85	285	MLA DEM
M-NSP82	61.59	59.32	593	MLA DEM
M-NSP83	92.68	75.75	268	MLA DEM
M-NSP84	95.54	79.02	488	MLA DEM
M-NSP85	120.08	73.18	249	MLA DEM

M-NSP86	109.79	70.29	298	MLA DEM
M-NSP87	67.27	56.83	252	MLA DEM
M-NSP88	62.11	56.79	179	MLA DEM
M-NSP89	48.18	39.42	262	MLA DEM
M-NSP90	-80.17	63.67	262	MLA DEM
M-NSP91	39.04	57.21	336	MLA DEM
M-NSP92	29.62	57.71	149	MLA DEM
M-NSP93	31.05	54.98	413	MLA DEM
M-NSP-94	4.92	82.98	155	MLA DEM
M-NSP95	80.47	38.14	232	MLA DEM
M-NSP96	78.16	44.70	559	MLA altimetry track - Oblique Traverse
M-NSP97	78.78	41.86	354	M3 DEM flyby
M-NSP-98	12.32	81.74	332	MLA DEM
M-NCCP1	-166.15	52.32	633.5	MLA DEM
M-NCCP2	-159.05	57.65	444	MLA altimetry track
M-NCCP3	-152.39	56.11	421.5	MLA DEM
M-NCCP5	-148.11	60.99	257	MLA DEM
M-NCCP6	-175.96	52.84	141	MLA DEM
M-NCCP7	131.31	52.32	237	MLA DEM
M-NCCP8	120.42	50.74	369	MLA DEM
M-CCP-1	151.36	8.29	558	MLA DEM
M-CCP-2	166.93	-7.17	166.5	MLA DEM
M-NCCP10	177.44	60.82	568.5	MLA DEM
M-ECCP-OP1†	-164.13	21.72	444	MLA altimetry track
M-ECCP-OP2†	-157.56	18.45	312	MLA altimetry track - Oblique Traverse
M-ECCP-OP3†	-155.20	13.00	233	MLA altimetry track - Oblique Traverse
M-ECCP-OP4†	-156.93	15.86	510	MLA altimetry track - Oblique Traverse
M-ECCP-OP5†	-167.42	19.98	243	MLA DEM
M-ECCP-OP6†	-167.99	31.13	383	MLA altimetry track - Oblique Traverse
M-ECCP-OP7†	-160.67	19.49	190	MLA altimetry track
M-SCCP1†	-175.44	10.79	467	MLA altimetry track - Oblique Traverse
M-SCCP3†	-172.47	0.66	574	MLA altimetry track - Oblique Traverse
M-SCCP4†	-173.00	0.50	234	MLA altimetry track - Oblique Traverse
M-SCCP5†	-176.96	14.04	455	MLA altimetry track - Oblique Traverse
M-WR-CB1	157.56	27.27	276	DLR Orbital DEM
M-WR-CB2	156.57	28.11	208	DLR Orbital DEM
M-WR-CB3	155.88	25.20	524	DLR Orbital DEM
M-WR-CB4	156.25	23.87	411	DLR Orbital DEM
M-WR-CB5	154.44	26.04	377	DLR Orbital DEM
M-WR-CB6	160.26	24.20	186	DLR Orbital DEM
M-WR-CB7	161.09	25.23	433	DLR Orbital DEM
M-WR-CB8	161.76	24.36	402	DLR Orbital DEM
M-WR-CB9	159.95	28.66	207	DLR Orbital DEM
M-WR-CB10	158.85	30.92	264	DLR Orbital DEM

M-WR-CB11	157.86	31.64	254	DLR Orbital DEM
M-WR-CB12	163.92	32.21	190	DLR Orbital DEM
M-WR-CB13	148.62	31.31	479	MLA altimetry track
M-WR-CB14	144.40	30.18	470	M1 DEM flyby
M-WR-CB15	143.70	26.62	485	MLA altimetry track
M-WR-CB16	146.50	23.28	238.5	MLA altimetry track
M-WR-CB17	148.44	25.23	243	M1 DEM flyby
M-WR-CB18	154.95	19.10	282	M1 DEM flyby
M-WR-CB19	167.65	17.80	400	M1 DEM flyby
M-WR-CB20	171.22	24.34	265	M1 DEM flyby
M-WR-CB21	176.23	24.60	318	M1 DEM flyby
M-WR-CB22	177.84	23.45	193	M1 DEM flyby
M-WR-CB23	-179.67	30.65	566.5	MLA altimetry track
M-WR-CB24	178.46	30.89	326	M1 DEM flyby
M-WR-CB25	179.93	34.89	565	M1 DEM flyby
M-WR-CB26	171.64	30.47	152.5	MLA altimetry track
M-WR-CB27	176.94	40.14	348	MLA altimetry track
M-WR-CB28	176.44	37.81	347	M1 DEM flyby
M-WR-CB29	171.63	38.86	284	M1 DEM flyby
M-WR-CB30	154.47	46.27	253	M1 DEM flyby
M-WR-CB31	153.31	42.80	437	M1 DEM flyby

[a]Wrinkle ridges are unofficially named for the purposes of this study using abbreviations based on their locations in basin or smooth plains material (NSP = northern smooth plains, NCCP = northern circum-Caloris plains, CCP = circum-Caloris plains, ECCP-OP = eastern circum-Caloris plains – Odin Planitia, SCCP = southern circum-Caloris plains, CB = Caloris basin interior)

[†]Wrinkle ridge previously identified from Mariner 10 and MESSENGER flyby imagery [*Watters et al.*, 2009c]

Table S2. Lunar wrinkle ridge locations and relief measurements

Lunar wrinkle ridge ID (informal)[a]	Longitude (°E)	Latitude (°N)	Relief (m)	Topographic data source
L-CR1	56.20	21.96	144	LOLA
L-CR2	60.45	21.11	100	WACDEM
L-CR3	62.96	21.62	420	WACDEM
L-CR4†	64.85	19.15	563	WACDEM
L-CR5†	64.86	18.71	268	WACDEM
L-CR6†	65.11	15.93	219	WACDEM
L-CR7†	63.65	13.86	526	WACDEM
L-CR8	60.87	13.32	81	WACDEM
L-CR9	57.20	11.68	257	LOLA
L-CR10	53.75	13.21	239	WACDEM
L-CR11†	52.04	15.74	341	WACDEM
L-CR12†	52.03	18.87	330	WACDEM
L-CR13	54.96	12.73	226	WACDEM
L-CR14	55.77	12.57	96	WACDEM
L-CR15	52.79	13.96	232	WACDEM
L-CR16†	59.77	22.31	205	WACDEM
L-CR17	53.40	21.54	101	WACDEM
L-CR18	53.95	19.98	47	WACDEM
L-CR19†	52.69	20.14	399	WACDEM
L-CR20	58.01	14.72	162	WACDEM
L-S1	9.55	26.19	127	LOLA
L-S2	8.12	23.43	171	WACDEM
L-S3	11.88	24.19	106	WACDEM
L-S4†	11.50	21.53	176	LOLA
L-S5	22.25	8.76	181	WACDEM
L-S6†	13.56	19.73	360	WACDEM
L-S7	14.18	18.47	127	LOLA
L-S8	23.95	20.52	292	WACDEM
L-S9	21.06	19.07	173	WACDEM
L-S10†	28.95	24.51	79	WACDEM
L-S11	19.88	19.27	283	WACDEM
L-S12	25.40	25.15	344	WACDEM
L-S13	24.85	29.19	275	WACDEM
L-S14	23.61	30.54	212	LOLA
L-S15	15.86	19.35	206	WACDEM
L-S16	21.42	32.48	261	LOLA
L-S17	20.47	33.71	84	WACDEM
L-S18	18.49	33.98	241	WACDEM
L-S19	15.01	30.59	98	WACDEM
L-S20	18.72	28.21	165	WACDEM
L-S21	25.54	27.04	244	WACDEM

L-S22	24.04	34.01	88	WACDEM
L-S23	8.41	29.24	113	WACDEM
L-S24	24.67	22.95	144	WACDEM
L-S25	25.33	30.64	307	WACDEM
L-S26	18.95	19.87	95	WACDEM
L-S27	22.74	18.10	157	WACDEM
L-I1	-25.58	44.70	140	WACDEM
L-I2	-20.15	47.24	432	LOLA
L-I3	-12.93	46.29	426	LOLA
L-I4	-4.73	45.15	236	WACDEM
L-I5	-8.25	40.97	271	WACDEM
L-I6	-7.67	22.42	151	WACDEM
L-I7	-12.43	29.23	159	LOLA
L-I8	-22.77	29.15	132	LOLA
L-I9	-24.51	29.22	378	LOLA
L-I10	-28.19	31.77	76	WACDEM
L-I11	-29.45	31.64	176	WACDEM
L-I12	-30.85	37.54	284	WACDEM
L-I13	-22.38	46.92	316	WACDEM
L-I14	-19.29	46.11	95	WACDEM
L-I15	-27.46	41.77	76	WACDEM
L-I16	-29.58	39.11	89	WACDEM
L-I17	-31.29	35.82	204	WACDEM
L-I18	-19.76	24.26	261	WACDEM
L-OP1	-53.18	50.89	155	WACDEM
L-OP2	-67.70	52.28	114	LOLA
L-OP3	-70.67	46.39	151	LOLA
L-OP4	-63.31	46.59	188	LOLA
L-OP5	-69.11	45.10	120	LOLA
L-OP6	-73.49	44.53	136	LOLA
L-OP7	-61.16	44.15	104	LOLA
L-OP8	-65.43	40.75	273	WACDEM
L-OP9	-60.38	38.23	208	WACDEM
L-OP10	-54.33	36.77	119	WACDEM
L-OP11	-61.15	36.38	85	WACDEM
L-OP12	-73.85	34.10	295	WACDEM
L-OP13	-61.37	34.65	172	WACDEM
L-OP14	-59.06	34.66	185	WACDEM
L-OP15	-59.91	32.16	156	WACDEM
L-OP16	-57.44	30.40	132	WACDEM
L-OP17	-57.01	28.62	122	WACDEM
L-OP18	-57.43	26.76	150	WACDEM
L-OP19	-56.61	25.57	255	WACDEM
L-OP20	-52.76	19.05	100	WACDEM

L-OP21	-38.33	18.93	193	LOLA
L-OP22	-64.33	19.20	79	WACDEM
L-OP23	-61.20	16.44	222	LOLA
L-OP24	-55.89	11.94	109	WACDEM
L-OP25	-57.05	10.14	146	WACDEM
L-OP26	-50.60	9.09	154	WACDEM
L-OP27	-50.19	8.52	205	WACDEM
L-OP28	-61.15	5.85	210	WACDEM
L-OP29	-61.66	4.46	102	WACDEM
L-OP30	-60.79	4.34	162	WACDEM
L-OP31	-60.69	3.49	268	WACDEM
L-OP32	-59.33	4.00	157	WACDEM
L-OP33	-57.90	1.52	210	WACDEM
L-OP34	-57.13	0.76	172	WACDEM
L-OP35	-54.99	-0.61	52	WACDEM
L-OP36	-56.23	-1.53	147	WACDEM
L-OP37	-57.58	-3.24	102	WACDEM
L-OP38	-55.35	-3.18	186	WACDEM
L-OP39	-50.62	5.36	204	WACDEM
L-OP40	-51.59	4.19	146	WACDEM
L-OP41	-50.77	3.06	64	WACDEM
L-OP42	-49.52	3.75	130	WACDEM
L-OP43	-48.82	5.13	82	WACDEM
L-OP44	-48.52	2.89	147	WACDEM
L-OP45	-48.43	1.25	110	WACDEM
L-OP46	-44.93	0.48	358	WACDEM
L-OP47	-51.54	-0.30	63	WACDEM
L-OP48	-50.71	-1.52	193	WACDEM
L-OP49	-49.17	-2.81	136	WACDEM
L-OP50	-35.32	-1.07	156	WACDEM
L-OP51	-32.17	-2.79	232	WACDEM
L-OP52	-34.06	-5.38	143	WACDEM
L-OP53	-54.86	4.80	178	WACDEM
L-FR1	-26.77	60.86	98	WACDEM
L-FR2	-20.92	59.81	256	LOLA
L-FR3	-16.99	62.28	204	LOLA
L-FR4	-14.33	61.10	391	LOLA
L-FR5	-3.74	59.42	70	LOLA
L-FR6	-3.75	58.18	252	LOLA
L-FR7	2.99	57.61	114	LOLA
L-FR8	10.64	55.45	199	WACDEM
L-FR9	25.03	56.02	89	LOLA
L-FR10	24.99	54.83	292	LOLA
L-FR11	35.53	54.46	126	LOLA

L-FR12	35.54	53.87	57	LOLA
L-FR13	35.54	53.54	146	LOLA
L-FR14	-1.73	56.77	63	WACDEM
L-FR15	-18.60	55.50	60	WACDEM
L-FR16	-14.64	56.22	146	WACDEM
L-FR17	-25.94	58.60	66	WACDEM
L-HU1†	-44.91	-23.58	361	WACDEM
L-HU2†	-44.20	-26.33	268	WACDEM
L-HU3	-37.72	-20.18	134	WACDEM
L-HU4†	-37.58	-27.32	307	WACDEM
L-HU5	-36.59	-24.57	117	WACDEM
L-HU6	-35.81	-22.66	233	WACDEM
L-FE1	49.43	-1.04	343	LOLA
L-FE2†	52.58	-4.41	636	WACDEM
L-FE3	52.63	-7.69	678	WACDEM
L-NU1	-10.19	-23.79	300	WACDEM
L-NU2	-24.75	-25.56	224	WACDEM
L-NU3	-11.99	-18.45	115	WACDEM
L-T1	28.44	2.78	144	LOLA
L-T2	22.08	3.79	351	WACDEM
L-NE1†	38.54	-16.65	446	WACDEM

[a]Wrinkle ridges are unofficially named for the purposes of this study using abbreviations based on their basin location or nearby craters (L = Lunar, CR = Mare Crisium, S = Mare Serenitatis, I = Mare Imbrium, OP = Oceanus Procellarum, FR = Mare Frigoris, HU = c, FE = Mare Fecunditatis, NU = Mare Nubium, T = Mare Traniquillitatis, NE = Mare Nectaris)

†Elevation offset wrinle ridges

Table S3. Relief measurement uncertainties from different elevation data sources

Location	Source	Number	Vertical precision (m)	Relief uncertainty (m)
Mercury	MLA altimetry tracks	60	< 1	< 2
Mercury	MLA DEM	58	< 1	< 2
Mercury	Flyby and orbital stereo-derived DEMs	32	± 135	± 270
Moon	LOLA altimetry tracks	33	± 0.10	± 0.20
Moon	WAC stereo-derived DEM	117	± 10	± 20

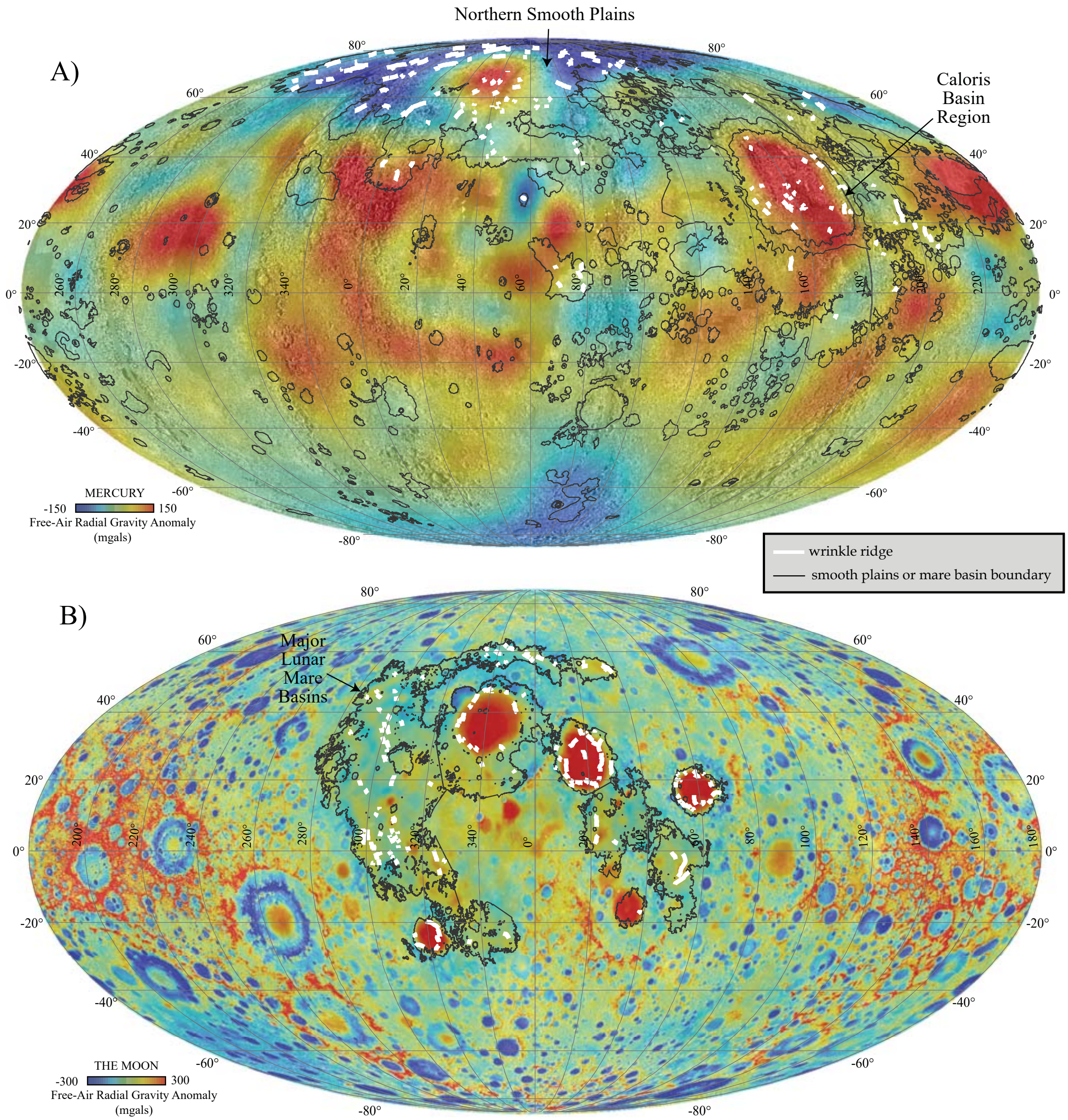

Figure 1 (Schleicher et al.)

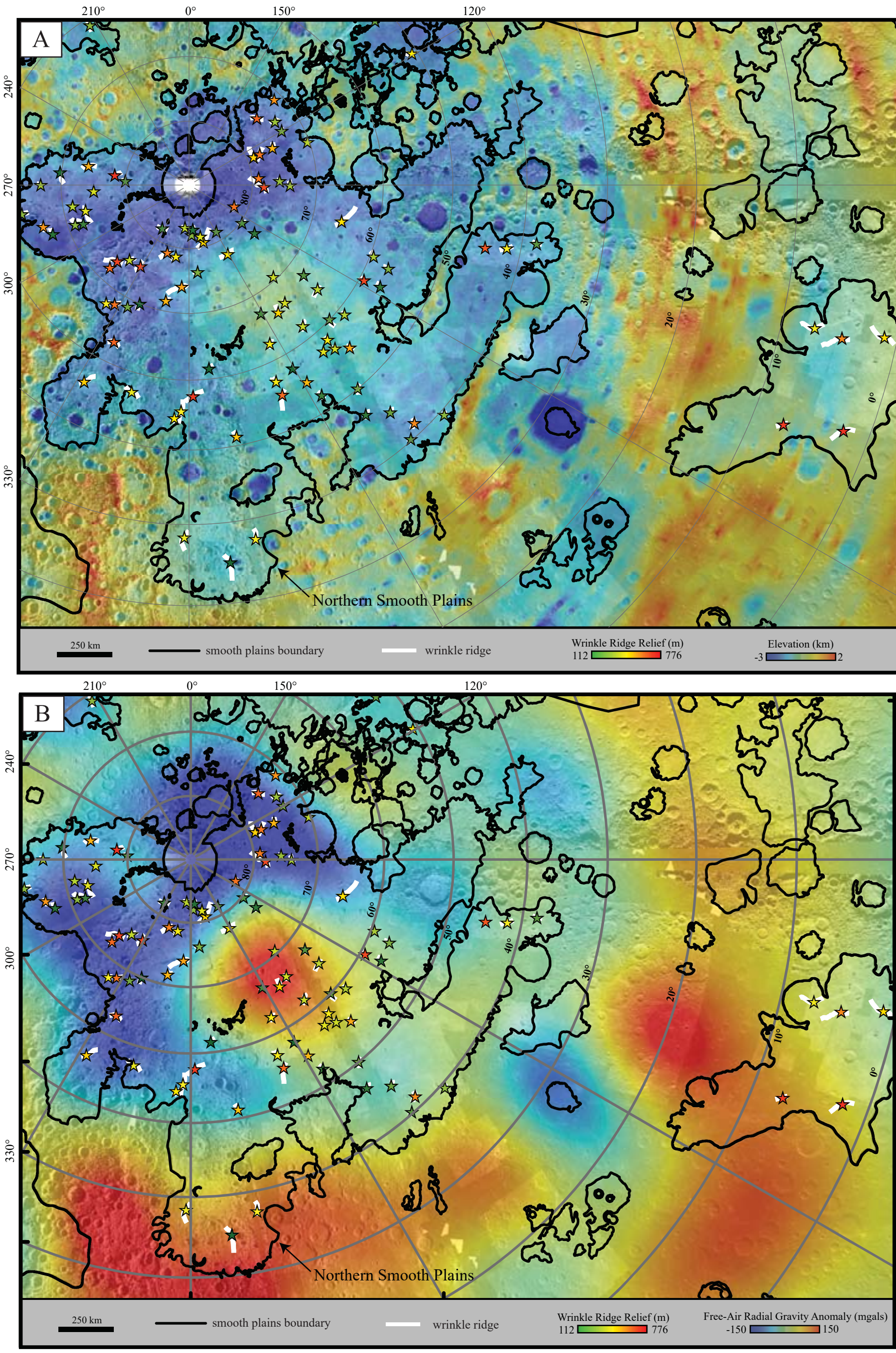

Figure 2 (Schleicher et al.)

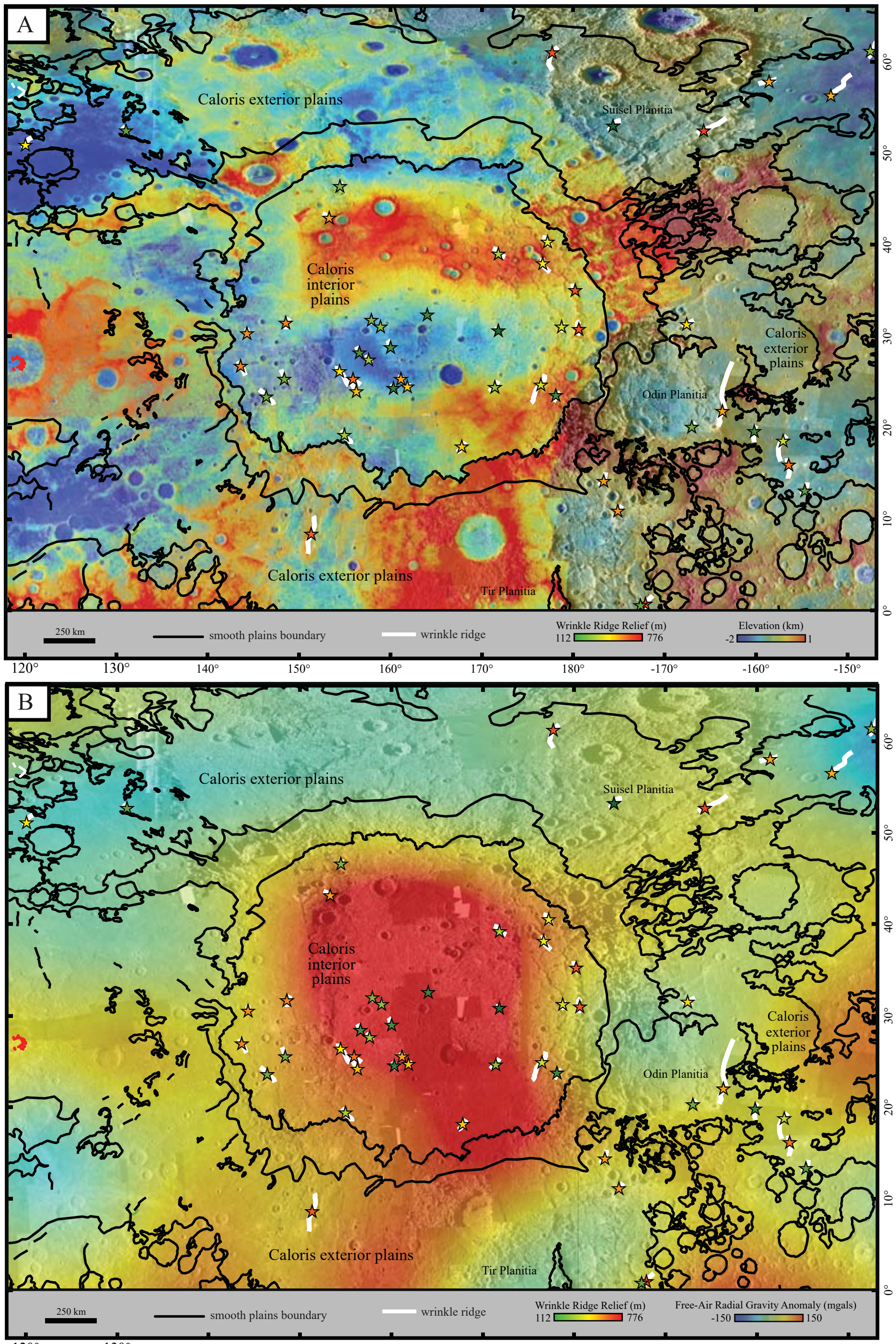

Figure 3 (Schleicher et al.)

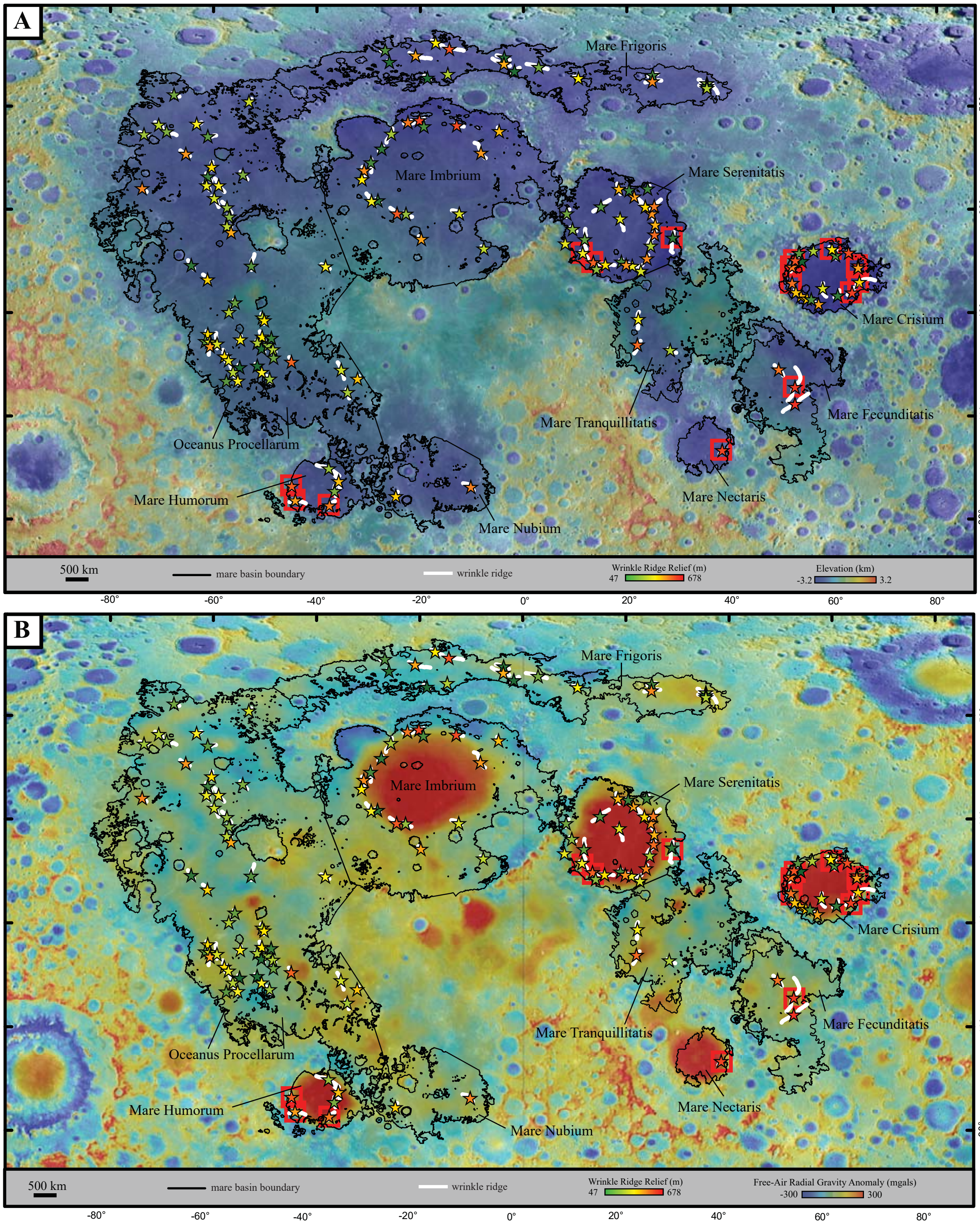

Figure 4 (Schleicher et al.)

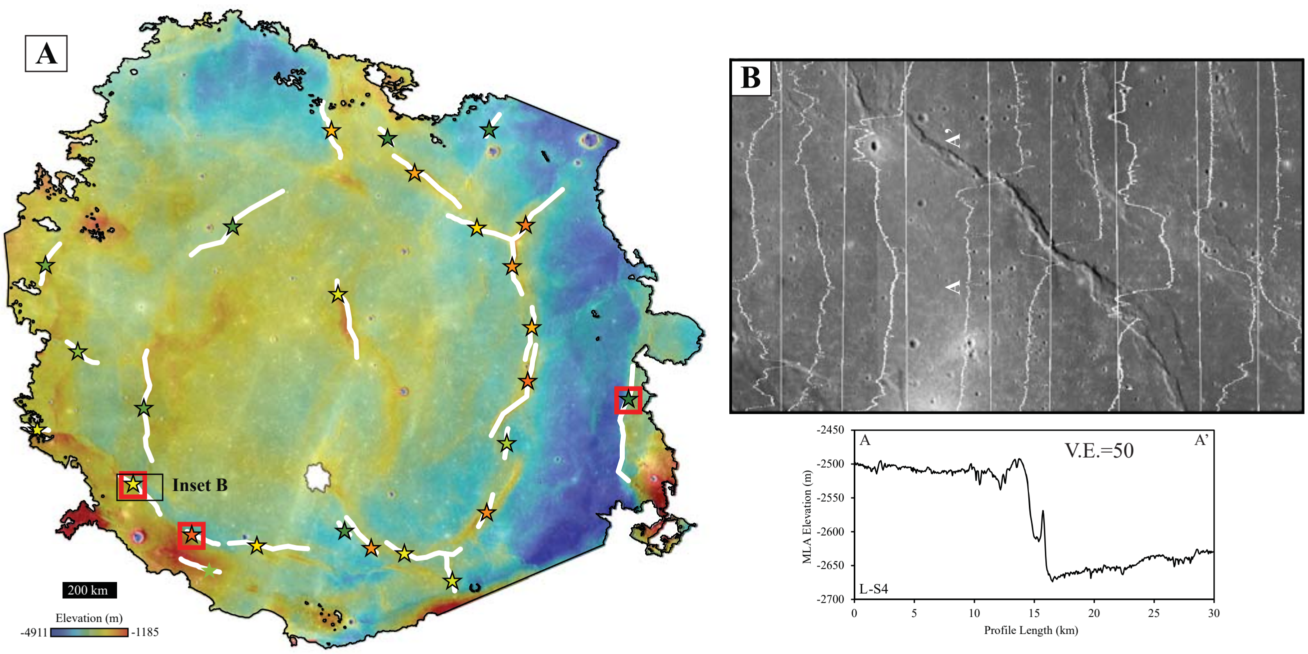

Figure 5 (Schleicher et al.)

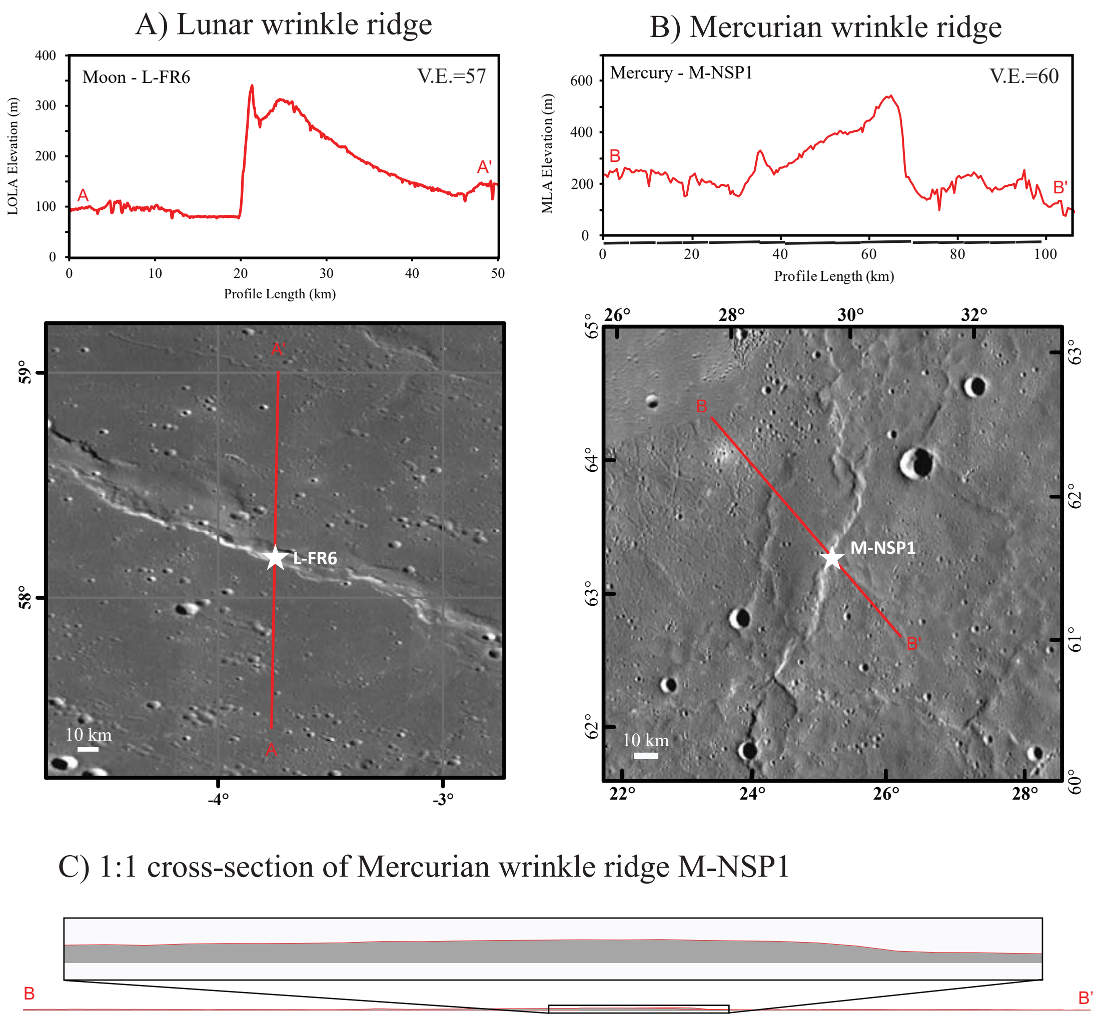

Figure 6 (Schleicher et al.)

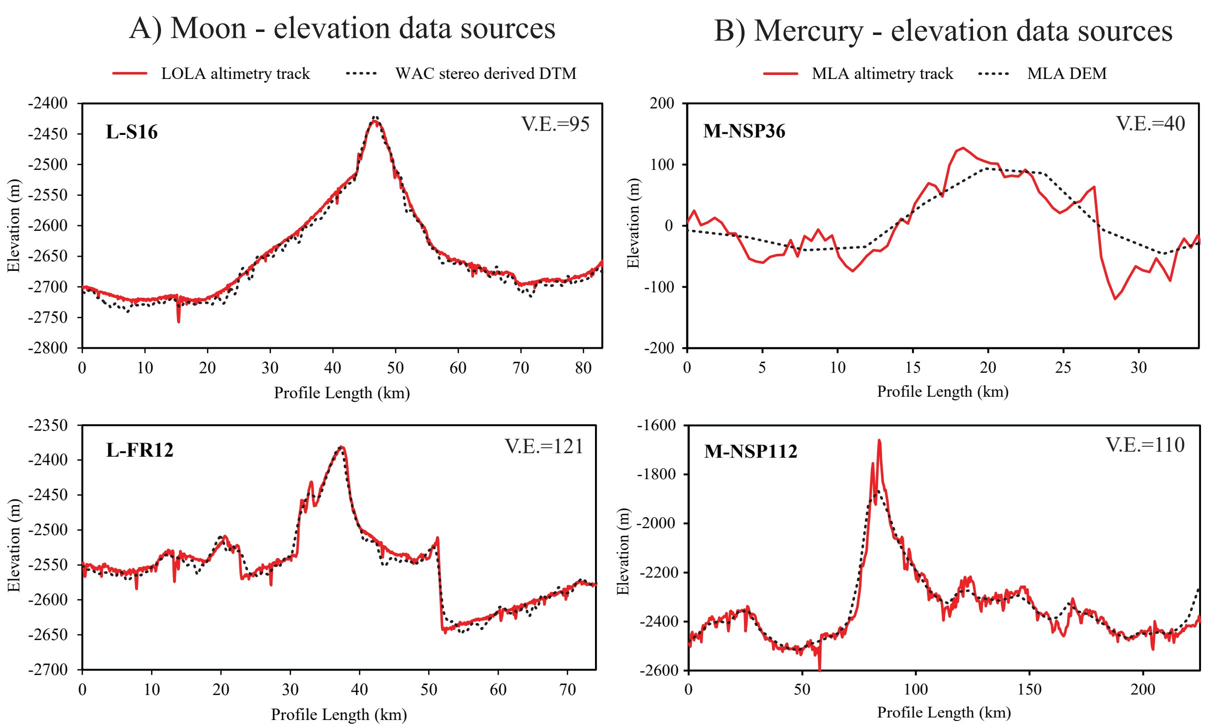

Figure 7 (Schleicher et al.)

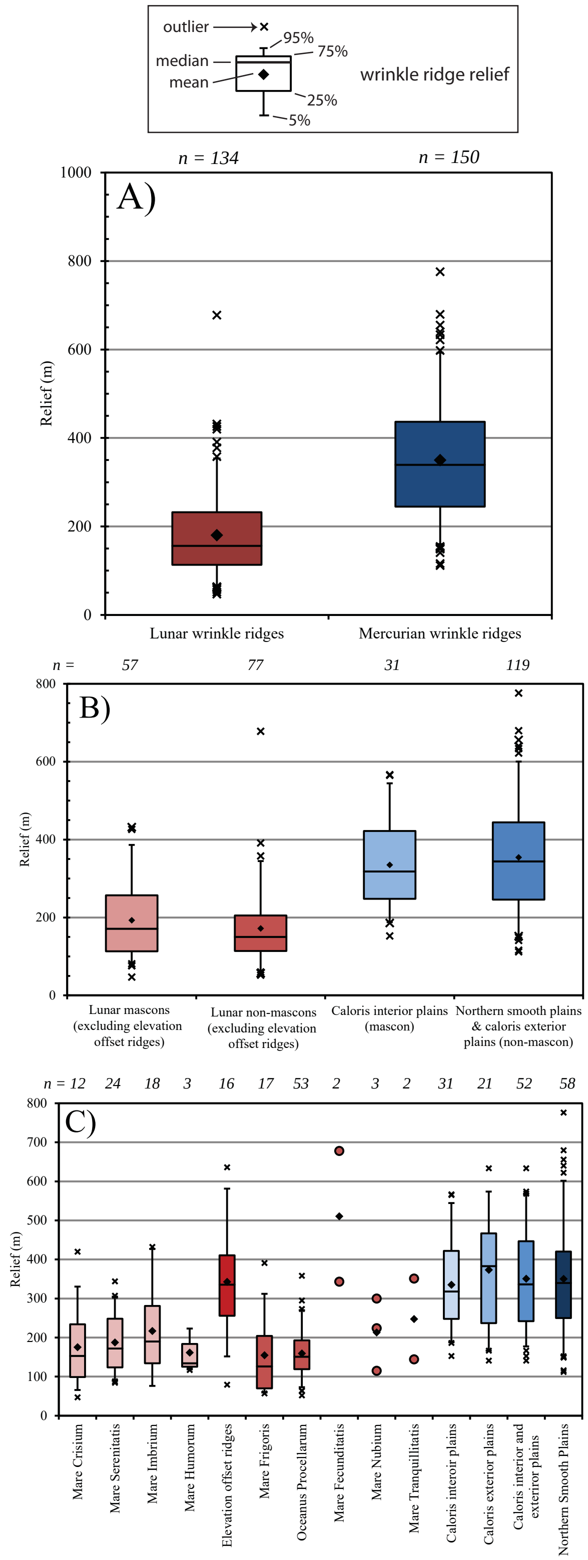

Figure 8 (Schleicher et al.)

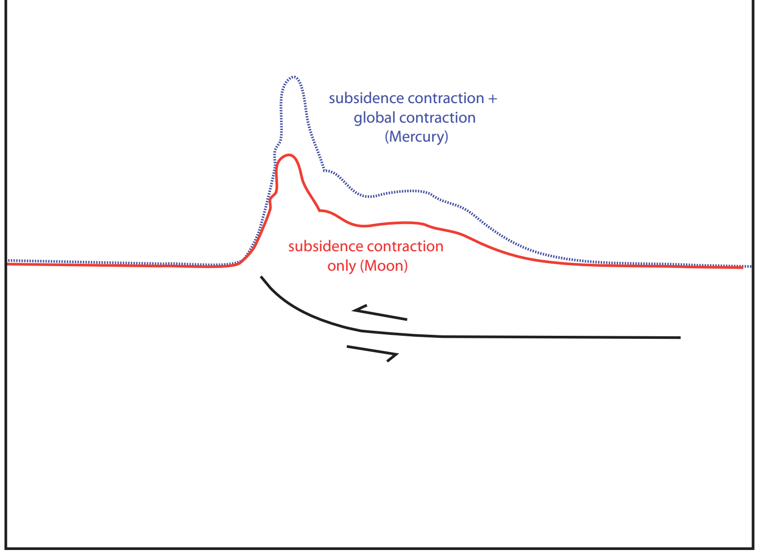

Figure 9 (Schleicher et al.)

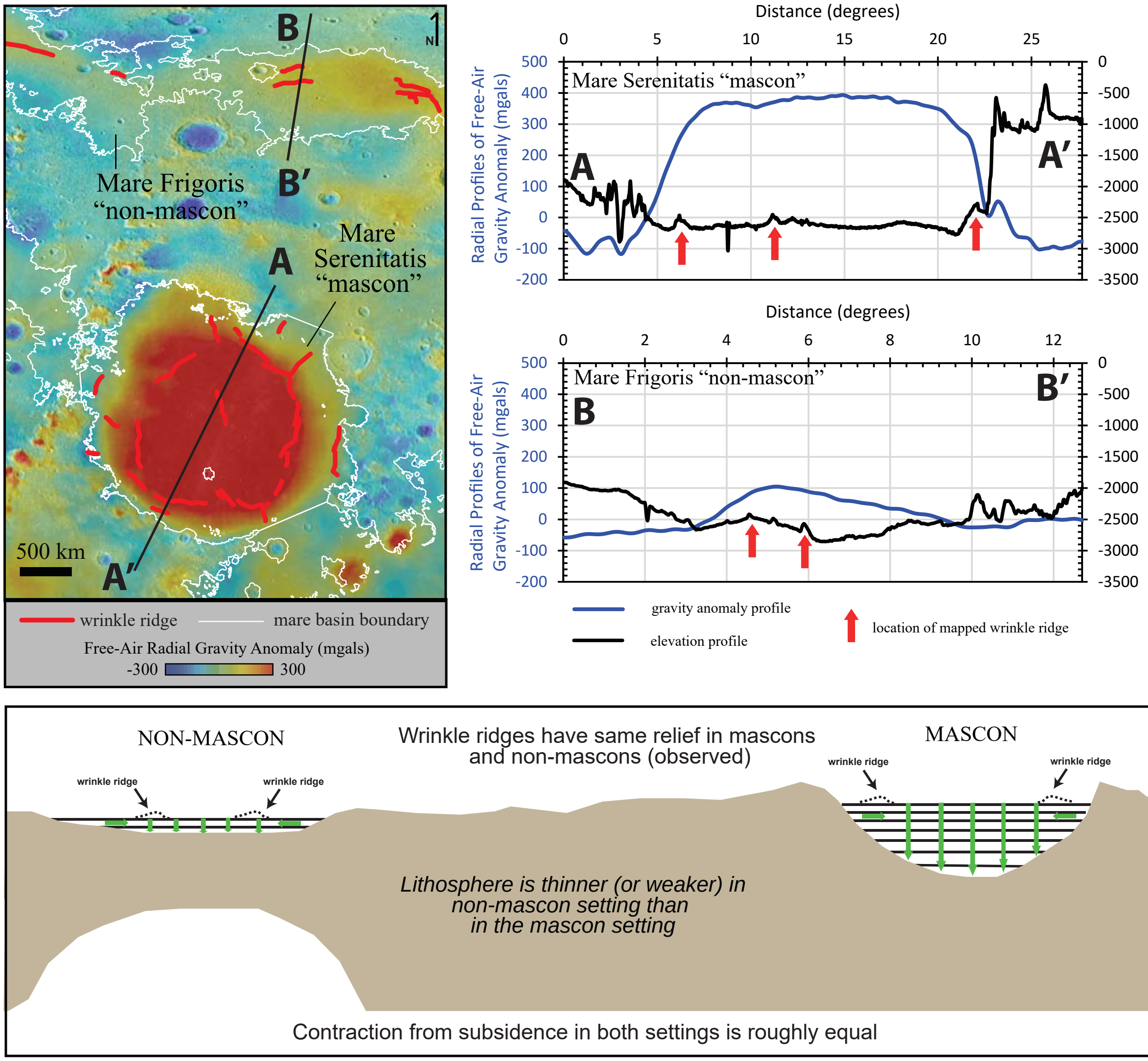

Figure 10 (Schleicher et al.)